Study of turbulence-radiation interactions in a heated jet using direct numerical simulation coupled to a non-gray Monte-Carlo solver

J.M. Armengol, Ronan Vicquelin, Axel Coussement, R.G. Santos, Olivier Gicquel

J.M. Armengol, Ronan Vicquelin, Axel Coussement, R.G. Santos, Olivier Gicquel. Study of turbulence-radiation interactions in a heated jet using direct numerical simulation coupled to a non-gray Monte-Carlo solver. International Journal of Heat and Mass Transfer, 2020, 162, pp.120297 -. 10.1016/j.ijheatmasstransfer.2020.120297 . hal-03492226

Version of Record: https://www.sciencedirect.com/science/article/pii/S0017931020332336
Manuscript_8bb0e29689c9c656a6c3e50d2e94aa86

Study of turbulence-radiation interactions in a heated jet using Direct Numerical Simulation coupled to a non-gray Monte-Carlo solver

J.M. Armengol[a,c], R. Vicquelin[a,*], A. Coussement[b], R.G. Santos[c], O. Gicquel[a]

[a] *Laboratoire EM2C, CNRS, CentraleSupélec, Université Paris-Saclay, Gif-sur-Yvette, France*
[b] *Aero-Thermo-Mechanics Laboratory, Ecole Polytechnique de Bruxelles, Université Libre de Bruxelles, Bruxelles, Belgium*
[c] *Faculty of Mechanical Engineering, University of Campinas (UNICAMP), Campinas-SP, Brazil*

Abstract

Direct Numerical Simulations of a strongly heated jet of water vapor discharging into a low-speed coflow of cold water vapor is fully coupled with a reciprocal Monte-Carlo method to account for radiative heat transfer. The spectral dependency of the radiative properties is modeled using the Correlated-k method. Such a numerical and modeling setup allows for studying accurately the turbulent jet development submitted to radiative heat transfer. Contrary to the previous study by Armengol *et al.* [International Journal of Heat and Mass Transfer 139 (2019), pp. 456-474], the present conditions show a direct effect of thermal radiation in the jet developed zone located downstream the jet potential core. Results are analyzed to identify the effects of thermal radiation on turbulence properties of the temperature field, and reciprocally. The analysis reveals a complex coupling between the mean temperature field and the mean radiative power as well as between their fluctuations. This is studied in various profiles of average and root-mean-square properties, and completed by considering budgets of enthalpy variance and turbulence spectra.

Keywords: `Turbulence-Radiation Interactions, Turbulent Jet, Direct Numerical Simulation, Thermal Radiation, Monte Carlo Method.`

---

1. Introduction

Thermal radiation plays an important role in a broad range of thermal engineering applications comprising turbulent flows such as combustion, propulsion, or environmental flows. In such applications, radiation modifies heat transport and fluid dynamics, while turbulence fluctuations can significantly alter the radiative heat transfer. Those interactions are commonly called turbulence-radiation interactions (TRI) [1, 2]. In a broad sense, this stands for effects that turbulence causes on thermal radiation and vice-versa.

Turbulence effects on thermal radiation arise from fluctuations of temperature and species concentration. When computing the mean radiative fields from averaged quantities in a turbulent participating media, results may significantly differ from the average radiative solution obtained using

---

Preprint submitted to International Journal of Heat and Mass Transfer * Corresponding author *July 17, 2020* instantaneous values directly. Modeling turbulence through average operations (same for filtering in large-eddy simulations) gives rise to two unclosed terms in the radiative transfer equation (RTE). In the combustion framework, many authors have demonstrated the importance of these terms related to TRI [3–6]. Acknowledging this effect, several works on coupled simulations using Reynolds average Navier-Stokes (RANS) have accounted for the impact of turbulence on the computation of the mean radiative power field [5, 7, 8]. More recently, relying on large-eddy simulations to directly capture turbulence-radiation interactions at the resolved scales has become more and more popular [9–14].

The latter studies can consider rather complex configurations, which makes it challenging to analyze the interplay between thermal radiation and turbulence. Several studies based on non-reactive flows have then been considered for such a fundamental analysis. The analyzed nonreactive systems include homogeneous isotropic turbulence [15–18], free shear flows (temporally evolving jet [19], mixing layer [20]) or channel flows [21, 22]. These studies rely mostly on uncoupled simulations, while others [20, 22] have considered coupled large-eddy simulations where the turbulent eddies are not fully resolved. In this nonreactive framework, TRI effects on mean radiative fields are found to be minor although they increase along with the magnitude of turbulent fluctuations.

Regarding the reciprocal effects that thermal radiation can cause on turbulence properties, a dynamic coupling between radiation and turbulence is needed rather than a priori analysis. Hence, investigations with coupled direct numerical simulations (DNS) allow for a fundamental understanding of how radiation eventually modifies turbulent transport. On the one hand, a variety of coupled DNS works together with the gray gas assumption have been performed on different systems: statistically 1-dimensional premixed [6, 23] and non-premixed [24, 25] flames, and nonreactive channel flow [26]. Although a fictitious gray gas gives trends on how turbulence structures behave on the presence of radiation, it is a wrong approximation for radiative properties of molecular gas in the majority of applications [27]. On the other hand, coupled non-reactive DNS with an accurate description of gas radiative properties have mainly considered a channel flow configuration [28–30]. These studies have observed that radiative transfer in the channel flow decreases temperature fluctuations and turbulent heat transfer. While smoothing temperature gradients, radiation decreases the thermal turbulent production due to opposing behaviors of gas-wall and gas-gas radiative contributions. The present work analyzes the radiation effects on the turbulence structures of a strongly heated jet, which is a canonical system of free shear flows. The goal is to isolate the gas-gas radiative contribution to give insight not only on radiation effects on free jets but also on the behavior of turbulent flows in general.

The spatial evolution of a strongly heated jet of water vapor discharged into a parallel low-speed coflow of cold water vapor is described with coupled DNS. The spectral dependency of radiative properties is accounted for using the Correlated-k (ck) method [31, 32], and the radiative transfer equation is solved numerically with a reciprocal Monte-Carlo method. Such a level of description guarantees a high-fidelity of the analyzed results. The authors have carried out the first simulation of such a configuration [33] to reveal that thermal radiation can have two kinds of effects on the jet temperature profile: a direct one from radiative energy transfer and an indirect one due to the modified flow density. The slightly heated jet presented in [33] shows the main effect of radiation around the jet inlet and a negligible impact further downstream in the fully developed zone. The temperature profile is, however, affected all along the jet centerline. In the work of [33], a new scaling law for free jets was then derived from accounting for the indirect effect on density issued from the jet inlet and correctly discriminate whether radiation modifies the heat transfer mechanisms in the jet developed region or not. This initial study was restricted to moderate coupled effects of radiative heat transfer in a slightly heated jet where only the indirect ones were present in the developed zone. The present objectives are twofold: (1) provide new reference results for a strongly heated jet configuration where direct effects are still controlling the downstream jet evolution; (2) thoroughly analyze these effects in the present case representative of a free shear flow.

The strongly heated jet configuration is presented in §2, where the numerical methods are also introduced. Then, after an assessment of the accuracy of the Monte-Carlo results in §3, coupled results of the radiative power field are analyzed in §4.1. The effects of radiation on mean temperature are studied in §4.2. In particular, the so-called direct effects of thermal radiation are revealed by the balance of mean enthalpy and the scaling derived in [33]. The temperature turbulent fluctuations are then examined in terms of root-mean-square, the budget of enthalpy variance, and turbulence spectra in Secs. 4.3 and 4.4. Finally, quantification of TRI effects on turbulent heat transport and mean radiation is presented in Secs. 4.5 and 4.6.

2. Problem description

2.1. Physical configuration

The jet evolves from the inlet section ($x = 0$) in an initial zone which includes the potential core region followed by the interaction of two separated shear layers before eventually reaching the developed turbulent zone. In the fully developed zone, universal self-similarity is expected for velocity and temperature profiles, when adequately scaled, in incompressible flows [34]. The streamwise direction is here x, the cross-stream coordinate is y, and z is the spanwise direction. The turbulent statistics of a plane jet are stationary, two-dimensional, and present a symmetry about the plane $y = 0$.

The jet configuration, sketched in Fig. 1, is defined by the initial jet width δ, the inlet velocities (U_1, U_2) and temperatures (T_1, T_2), the mean pressure (P_0), and the Reynolds number based on the initial jet width $\mathrm{Re} = \rho(T_1)\Delta U_0 \delta/\mu(T_1)$ (where $\Delta U_0 = U_1 - U_2$, and $\rho(T_1)$ and $\mu(T_1)$ stand for density and viscosity evaluated at T_1). The value of all these parameters for the present simulation are specified in Table 1.

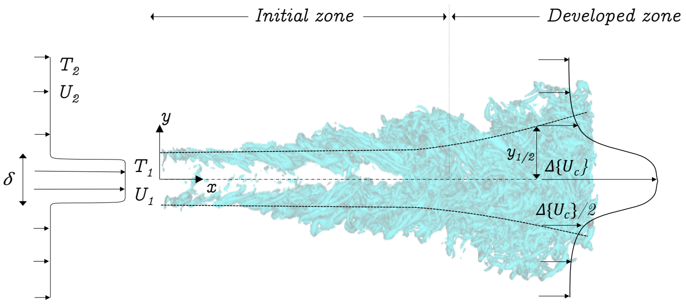

Figure 1: Schematic representation of the characteristic zones of a turbulent heated plane jet, the turbulent structures of the shear layers of the developing jet are identified by the Q-criterion.

Table 1: Configuration of the strongly heated jet.

δ [m]	U_1 [m/s]	U_2 [m/s]	T_1 [K]	T_2 [K]	P_0 [atm]	Re
5×10^{-2}	4.176	$U_1/10$	2500	405	2.576	500

The mixture composition is homogeneous and made of pure water vapor. The water vapor inlet temperature of the jet is set to $T_1 = 2500$ K based on temperature peak values found in combustion systems. T_2 is set to be close to the minimal temperature at which water vapor remains in the gas state at $P_0 = 2.576$ atm.

The selected Reynolds number is somewhat low compared with previous DNS studies of turbulent plane jets [33, 35, 36] for which the Reynolds number range between 1000 to 6000. First, let us remind that, contrary to round jets, the downstream Reynolds number based on the jet centerline velocity and half-width keeps increasing. Besides, the retained Reynolds number is close to the experimental study of [37], who reported a fully turbulent plane jet of a Reynolds number of 700. In the present work, the Reynolds number is kept low to afford the computational cost of a coupled simulation with spectral thermal radiation while featuring a turbulent flow, as further discussed in §4.

In Figure 1, the jet half-width $y_{1/2}(x)$ is represented. This distance characterizes the downstream jet growth, and it is used to scale self-similar cross-section profiles of the jet. It stands for the distance between the jet centerline and the point where the **mean velocity corrected by the coflow velocity ($\{U_e\} = \{u\} - U_2$) is half of the value at the jet centerline ($\Delta\{U_c\} = \{U_c\} - U_2$), i.e., $\{U_e(x, y_{1/2})\} = \frac{1}{2}\Delta\{U_c(x)\}$.** Here the operation $\{\phi\}$ stands for the time Favre averaging of a variable ϕ. Also, further in the text, $\langle\phi\rangle$ refers to the Reynolds averaging operation. Additionally, ϕ' and ϕ'' denote respectively the Reynolds and Favre average fluctuating parts.

2.2. Fluid flow simulation

Except for the grid spacing used for the present configuration, the parameters of the flow simulation are identical to the ones used in [33]. They are briefly reminded for the sake of completeness. The set of equations that describe the plane jet are the Navier-Stokes equations for a compressible fluid in which gravitational effects are not considered:

$$\frac{\partial \rho}{\partial t}+\frac{\partial\left(\rho u_i\right)}{\partial x_i}=0, \tag{1}$$

$$\frac{\partial \rho u_j}{\partial t}+\frac{\partial\left(\rho u_i u_j\right)}{\partial x_i}=-\frac{\partial p}{\partial x_j}+\frac{\partial \tau_{ij}}{\partial x_i}, \tag{2}$$

$$\frac{\partial \rho e_t}{\partial t}+\frac{\partial\left(\rho e_t u_i\right)}{\partial x_i}=-\frac{\partial (p u_j)}{\partial x_j}+\frac{\partial (\tau_{ij} u_i)}{\partial x_j}-\frac{\partial q_i}{\partial x_i}+P_{rad}, \tag{3}$$

where ρ, t, u, p, τ_{ij}, e_t and q_i stand for density, time, instantaneous velocity, pressure, stress tensor, total energy and conductive heat flux vector, respectively. The source term P_{rad} is the radiative power per unit volume, further discussed in §2.3. The viscous stress tensor $\tau_{i,j}$ is defined as

$$\tau_{ij}=\mu\left(\left(\frac{\partial u_i}{\partial x_j}+\frac{\partial u_j}{\partial x_i}\right)-\frac{2}{3}\delta_{ij}\frac{\partial u_k}{\partial x_k}\right), \tag{4}$$

where μ is the dynamic viscosity and δ_{ij} is the Kronecker delta operator. The conductive heat flux vector q_i writes

$$q_i=-\lambda\frac{\partial T}{\partial x_i}, \tag{5}$$

where λ and T denote thermal conductivity and temperature, respectively. The energy transport is defined based on the total energy e_t, which accounts for the sum of internal and kinetic energies: $e_t=\frac{1}{2}u_i u_i+e$, where e is the internal energy. The enthalpy is denoted by $h=e+rT$ where $r=R/W$, R is the universal gas constant, and W stands for the molar weight of the mixture. The ideal gas equation is here used to compute pressure as $p=\rho r T$. Similar to [33], the transport properties of water vapor μ and λ are computed based on the data of Lemmon *et al.* [38], while heat capacity is assumed constant.

A fourth-order centered finite-difference scheme is used to discretize Eqs. 1 to 3. Time integration is performed using an explicit fourth-order Runge-Kutta. An implicit filter of 8^{th}-order [39] is used to damp high-wavenumber noise, enhancing the robustness of the solution. To reduce computational costs, the acoustic speed reduction (ASR) method [40], already used in the jet configuration [33], is adopted in the present work. The time step is then enlarged by the accelerator factor α set to

$\alpha = 6.82$. This value sets the Courant- Friedrichs-Lewy and the Fourier conditions within the same order of magnitude for the current simulation.

Boundary conditions are imposed using the Navier-Stokes Characteristic Boundary Conditions method [41] while using the modified sound speed consistently with the ASR method. Constant pressure is imposed at the outlets through a partially reflecting boundary condition. Inlet velocity and temperature profiles are defined using hyperbolic functions:

$$U_{in}(y) = \frac{U_1 + U_2}{2} + \frac{U_1 - U_2}{2} \tanh\left(\frac{\delta/2 - |y|}{2\theta}\right), \tag{6}$$

$$T_{in}(y) = \frac{T_1 + T_2}{2} + \frac{T_1 - T_2}{2} \tanh\left(\frac{\delta/2 - |y|}{2\theta}\right), \tag{7}$$

with a corresponding shear layer momentum thickness of $\theta = 0.02\delta$ following previous values [33, 35]. As discussed in [33], **synthetic turbulence is added to the inlet mean velocity at the jet region to destabilize the potential core, which shortens the domain needed to observe the jet developed zone. The Passot Pouquet model [42] is used to generate the synthetic turbulence setting a characteristic length of $\delta/2$ and a turbulent velocity of $u' = U_1/20$.**

The grid spacing in $x-$ and $y-$ axes are set from the approximate local Kolmogorov scale estimated from scaling laws for temperature and velocity fields [33]. For the spanwise direction z, the grid spacing is uniform and equal to $\Delta z = \delta/40$, based on the Δx and Δy averages. The flow solution is computed in a domain extension $(L_x \times L_y \times L_z)$ of $13.5\delta \times 10\delta \times 3\delta$ in x, y and z directions, respectively. A structured grid is used with $514 \times 401 \times 121$ nodes, in the x, y, and z directions, respectively, which corresponds to approximately 24.9×10^6 nodes. The statistics of the flow are computed in a domain extension of $10\delta \times 10\delta \times 3\delta$.

2.3. Radiation simulation

The Radiative Transfer Equation (RTE) is here numerically solved using a Monte-Carlo method. The RTE in an emitting-absorbing and non-scattering medium assuming local thermodynamic equilibrium can be expressed as

$$\frac{dI_\nu}{ds} = -\kappa_\nu I_\nu + \kappa_\nu I_{b\nu}, \tag{8}$$

where κ_ν stands for the absorption coefficient at a given wavenumber ν, I_ν is the local spectral radiative intensity, and $I_{b\nu}$ is the equilibrium spectral intensity given by Planck's law. The volumetric radiative power is a balance between the power lost by radiative emission P_e and the gained power due to radiative absorption P_a, i.e., $P_{rad} = P_a - P_e$. They are defined as

$$P_e = 4\pi \int_{\nu} \kappa_{\nu}(T) I_{b\nu}(T) d\nu, \quad P_a = \int_{\nu} \left(\kappa_{\nu}(T) \int_{4\pi} I_{\nu} d\Omega \right) d\nu. \tag{9}$$

An efficient Monte-Carlo method [43] is used in this study to determine the radiative power. It relies on an Emission-based Reciprocity method (ERM) [44] and takes advantage of a randomized Quasi Monte-Carlo (QMC) method [45]. The randomized QMC reduces the required computational time by sampling the random numbers using low-discrepancy Sobol sequences [46] to accelerate the statistical convergence. As the radiative power is determined at computational nodes, the statistical behavior is only based on three probability density functions: two to determine the direction (azimuthal and polar angles) and one to determine the wavenumber of the emitted ray, ν. For each ray, three pseudo-random numbers are generated using the randomized QMC method. Further details can be found in the work of Palluotto *et al.* [43].

The correlated-k (ck) narrowband model [31, 32] is here used to account for the spectral radiative properties of H_2O. Such a level of description is deemed very accurate for the targeted coupled simulations compared to Weighted-Sum-of-Gray-Gases (WSGG) global models or notoriously wrong gray-gas assumptions. The present ck model is based on updated parameters of Rivière and Soufiani [47]. For H_2O, these parameters are generated for 44 spectral bands (widths varying from 50 cm^{-1} to 400 cm^{-1}) and for a 300 - 4000 K temperature range. With 7-points Gauss-Lobatto quadrature points per band, the ck database is made of a total of 308 pseudo-spectral points. The accuracy of the ck model is further discussed in §3.1.

To keep affordable simulations in terms of time processing, the mesh to compute the radiative problem is based on a coarser mesh by considering one out of two nodes in each direction of the DNS mesh. Thus, the radiative mesh has $282 \times 235 \times 75$ grid nodes in the x, y and z directions, respectively. The affected accuracy due to this choice is analyzed in §3.1 for the present strongly heated jet.

One of the advantages of the retained ERM method is that only the bundles leaving a specific node are needed to estimate the local radiative power at this specific node. It is, therefore, possible to estimate the radiative power at one node without performing such estimation at all other nodes of the domain. The radiative power is only computed at relevant points to save computational time. The cross-stream coordinate y of these points is restricted to the range $[-4y_{1/2}(x), 4y_{1/2}(x)]$. Then, radiative calculations are only performed in a volume that surrounds the jet.

Periodic boundary conditions for the radiative solver are considered in the spanwise direction. Then, when a ray reaches a periodic boundary, say at the point (x, y, L_z), it continues propagating in the same direction at the point $(x, y, 0)$. The rest of the boundaries are assumed black-surfaces at the local temperature.

The Monte-Carlo solutions are considered converged when the relative standard deviation of the local estimated radiative power is lower than 5%, or the absolute standard deviation of the local estimated radiative power is lower than 0.5% of the maximum value in the magnitude of the radiative power in the domain. If these two criteria are not achieved, a maximum number of 2.5×10^3 rays is considered. This choice of the convergence criteria is also analyzed in §3.1.

The radiative power field is computed every 30 iterations of the fluid flow solver. This coupling period keeps the error associated with the coupling procedure below 5%. Details of the coupling error computation can be found in [33]. Once the coupling period is fixed, the number of processors dedicated to each code should be set to minimize the time spent on waiting for communications among processors.

3. Assessment of the Monte-Carlo computations

3.1. Accuracy of the computed radiative power field

The ck model used to estimate the spectral radiative properties of water vapor is first validated by comparison with line-by-line (LBL) results presented in the work of Soufiani and Taine [48] and results using the LBL database HITEMP [49] updated by Rivière and Soufiani [47]. Figure 2 compares LBL results [48, 49] of the transmissivity of an isothermal and homogeneous $H_2O - N_2$ ($X_{H_2O} = 0.5$) column of length $l = 0.5$ m at 1000 K with the results obtained using the present ck model. For this specific mixture, a good agreement between both approaches is observed over all the spectrum.

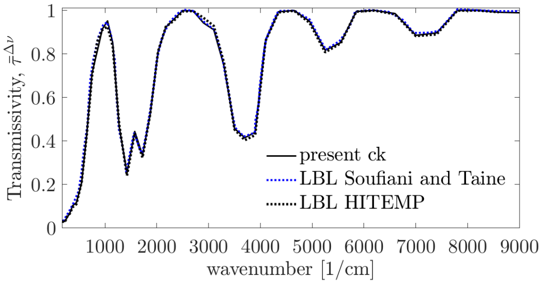

Figure 2: Comparison of the present ck model with LBL data from Soufiani and Taine [48] and HITEMP [49] for the spectral transmissivity of an isothermal and homogeneous column $X_{H_2O} = 0.5$ of length $l = 0.5$ m at 1000 K and pressure of 1 atm.

The ck model has also been compared with LBL results [47] for representative conditions of the present case. Figures 3a, 3b and 3c compare the transmissivity of a water vapor column of length $l = 0.05$ m at 405, 1452 and 2500 K, respectively, between the current ck model and the updated LBL database HITEMP [47]. For the three analyzed temperatures, the current ck model is in excellent agreement with LBL results over all the spectrum despite small differences that can be observed for the high-temperature case.

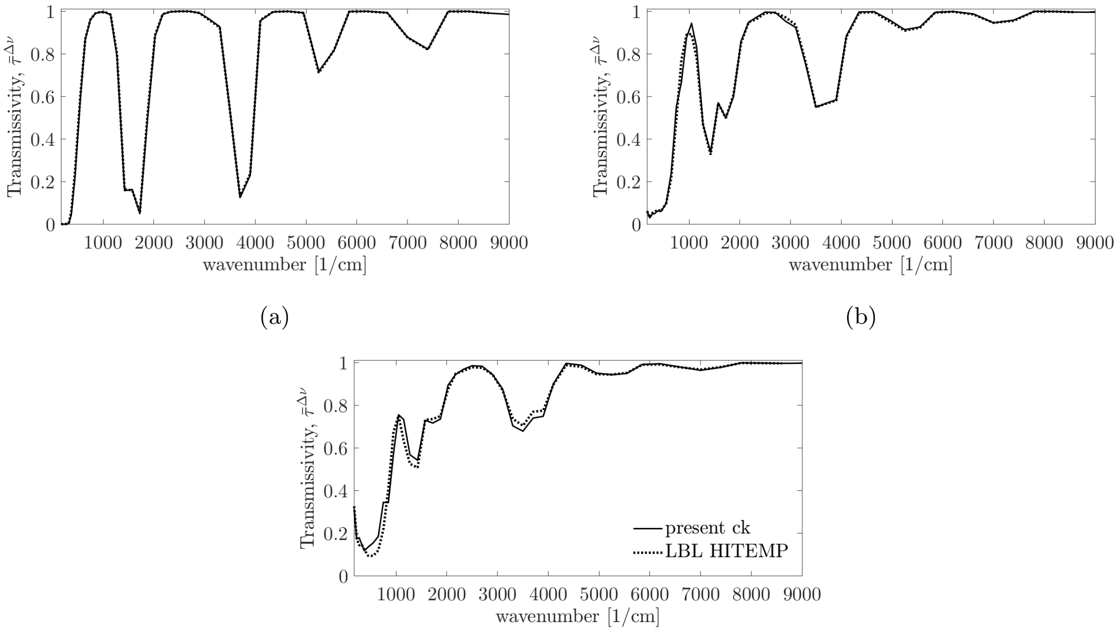

(a)

(b)

(c)

Figure 3: Comparison of ck model results of the spectral transmissivity of an isothermal and homogeneous water vapor ($X_{H_2O} = 1$) column of length $l = 0.05$ m at a pressure of 2.576 atm with LBL data (HITEMP [49]) for temperatures (a) 405 K, (b) 1452 K and (c) 2500 K.

Results varying key parameters of the Monte-Carlo solver are here analyzed to assess the accuracy of the radiative power field calculations. First, the effects of increasing the maximum number of rays issued from a node are analyzed. To do so, the radiative power field has been computed for a given instantaneous temperature field by setting the maximum number of rays to 2.5×10^3 and 5×10^3 while keeping constant all other parameters, including convergence criteria. Figure 4 shows instantaneous slices of the radiative power when a maximum number of rays of 2.5×10^3 and 5×10^3 are set. No significant qualitative differences can be observed in the radiative power field in Fig. 4. Additionally, downstream and cross-section profiles of the instantaneous radiative power are shown in Fig. 5a and Fig. 5b. It can be seen that, despite some small relative differences between both cases, a maximum number of 2.5×10^3 rays captures the trends of the radiative power accurately. Hence, a maximum number of 2.5×10^3 rays has been retained to control the amount of computation time with the available resources.

Secondly, the effects of considering a coarser mesh for the radiative computations are also analyzed. The coarse radiative mesh consists in $257 \times 201 \times 61$ grid nodes while the DNS fluid flow uses a mesh

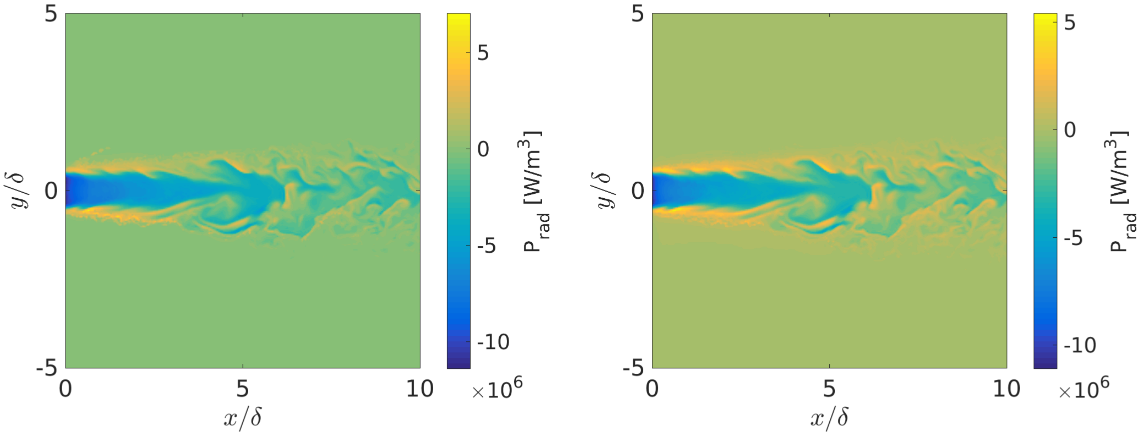

(a) (b)

Figure 4: Instantaneous radiative power field at $z = 0$ when a maximum number of 2.5×10^3 (a) and 5×10^3 (b) rays are issued form each node.

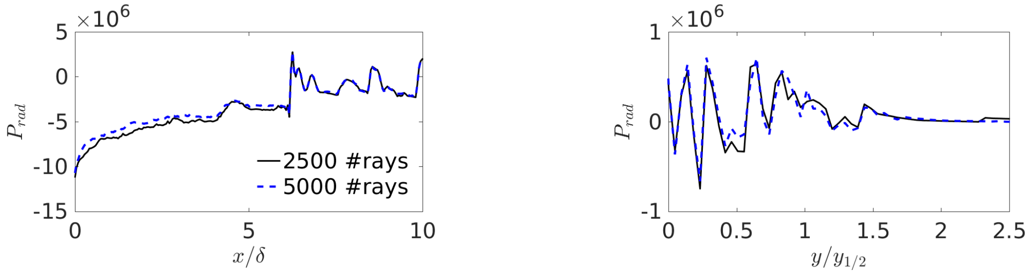

(a) (b)

Figure 5: Comparison between radiative power results for a maximum number of 2.5×10^3 and 5×10^3 issued form each node. (a) Downstream evolution of the radiative power and (b) cross-section profiles of radiative power at $x = 10\delta$.

with 514×401×121 nodes along x, y and z directions, respectively. To assess the independence of the radiative solution from the used mesh, radiative power fields have been computed using the DNS and coarser radiative meshes for a given instantaneous temperature field. Downstream and cross-section profiles of the instantaneous radiative power for both meshes are compared in Fig. 6a and Fig. 6b, respectively. From these results, it can be seen that the coarse mesh can correctly capture the trends of the radiative power. Despite the minor inaccuracy, the coarse mesh is retained in this study since radiative computations on the DNS mesh increase by a factor of 8 the required computational memory and time processing when compared to the coarse mesh.

For the convergence criteria specified in §2.3 and a given instantaneous field of temperature, the local number of rays issued to compute the radiative power using the Emission-based Reciprocity Monte-Carlo Method is shown in Fig. 7a; while the relative statistical error of convergence, computed

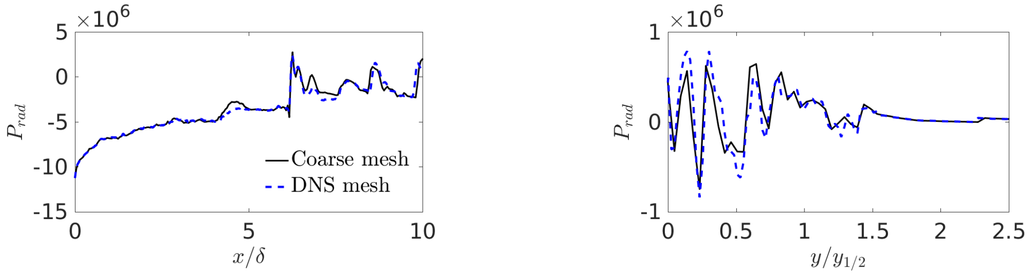

(a)

(b)

Figure 6: Comparison between radiative power results for the coarse and refined meshes. (a) Downstream evolution of the radiative power and (b) Cross-section profiles of radiative power at $x = 10\delta$

as the relative standard deviation of the local estimated P_{rad} (here denoted as P_{rad} rms), is presented in Fig. 7b.

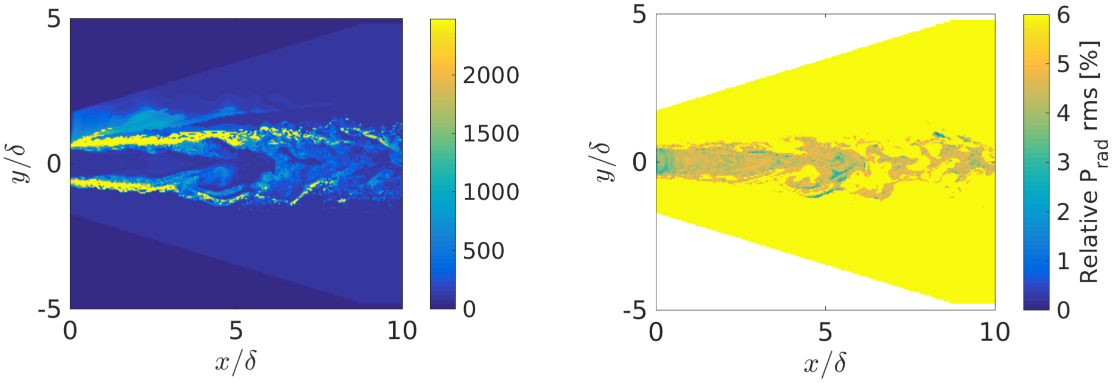

(a)

(b)

Figure 7: Contour fields at $z = 0$ related to the Monte-Carlo solution and its convergence. (a) Local number of rays and (b) Relative standard deviation (rms) of the radiative power statistical estimation.

As it can be seen in Fig. 7a, the jet edges are the hardest regions to converge the radiative power. Indeed, the radiative power in these regions is close to zero, which implies large values of the relative standard deviation of the local estimated radiative power. And, at the same time, this region has a strong radiative heat exchange with inner regions of the jet. Furthermore, regions with more than 5% of the relative standard deviation of estimated radiative power in Fig. 7b correspond to regions with P_{rad} close to zero. The computation stops in these regions because of the locally small absolute standard deviation or the reached maximum number of rays.

3.2. Nature of radiative transfer under the studied conditions

The radiative properties of a medium strongly affect the exchanged radiation and the behavior of TRI effects, as explained in the works of [1, 2]. The nature of the radiative transfer in the configuration under study is characterized by analyzing the spectral transmissivity of water vapor based on the initial jet width ($\delta = 0.05$ m).

The spectral transmissivity is computed using the ck model for the present temperature range (2500 K and 405 K) at a pressure of 2.576 atm and presented in Fig. 8a. Additionally, the spectral Planck functions for these temperatures are presented in Fig. 8b adimensionalized by its maximum value.

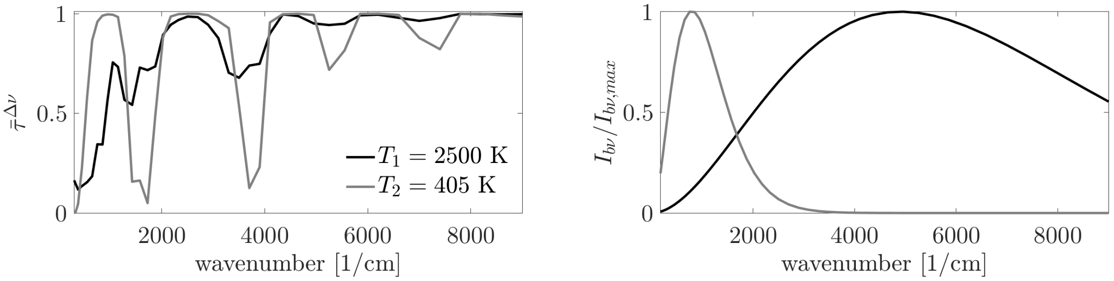

(a)

(b)

Figure 8: For a pressure of 2.576 atm and the maximum and minimum temperatures of the strongly heated jet: (a) spectral transmissivity of water vapor based on the initial jet width, and (b) spectral Planck functions adimensionalized by its maximum value.

From Fig. 8a, it can be seen that regardless of the temperature, water vapor tends to be optically thick at low wavenumbers ($\lesssim$ 500 cm^{-1}), and it presents two "peaks" of moderate-to-high optical thickness around wavenumbers of 1500 cm^{-1} and 3800 cm^{-1}. As temperature increases, these "peaks" of optical thickness decrease in magnitude. Additionally, Fig. 8b shows that temperature shifts the peak of emission towards higher wavenumbers and smooths the Planck function. Most of the emitted radiation comes from hot regions of the fluid, corresponding then to peaks at 1500 cm^{-1} and 3800 cm^{-1}). If the rays emitted in hot regions are not reabsorbed in the vicinity of the emission point, they are likely to be absorbed in the colder region, being that low-temperature fluid parcels have lower transmissivity values at these wavenumbers (1500 cm^{-1} and 3800 cm^{-1}), as shown in Fig. 8a. Finally, note that the presented radiative properties dependency on wavenumber points out the need to describe spectral properties. Here, a gray gas model cannot accurately account for radiative heat transfer.

4. Results of the heated turbulent jet coupled with thermal radiation

In this section, the effects of radiation on temperature and velocity fields are analyzed by comparing the heated jet without radiation **(NR)** and including radiation **(R)**.

The statistics are obtained by averaging the data over approximately $\tau = 1$ s of physical time. This time corresponds to approximately 4.6 flow time units defined as $\tau(U_1 + U_2)/(2L_x) = 4.6$, where L_x is the domain size in the x direction, $L_x = 10\delta$. The approximate total cpu cost of the coupled simulation using Intel Xeon CPU E5-2670 v3 24 cores @ 2.30 GHz is of 270000 h. The CPU time for the coupled simulation is approximately 3.3 times greater than the one for the simulation without radiation.

4.1. Radiative power field

Turbulent structures identified by the Q-criterion and colored by instantaneous emitted and absorbed power fields are shown in Fig. 9. A region with strong emission is identified close to the nozzle. Around the jet centerline, a peak of absorption is located δ downstream from the nozzle. Radiative power is the difference between emission and absorption. In order to analyze the net thermal radiation in the mean flow, the averaged radiative power $\langle P_{rad} \rangle$ is presented in Fig. 10. Regions with negative P_{rad} are losing energy by the effect of radiation, while regions with positive values are gaining energy due to radiation. The centerline of the jet mainly emits thermal radiation, and part of this radiation is further absorbed in colder regions of the jet. In Figure 10, the emission dominated region has been delimited from the absorption dominated region by solid black lines corresponding to isolines of $P_{rad} = 0$.

Figure 11a shows the downstream variation of the mean radiative emission and absorption powers along the centerline of the jet, both decrease in magnitude beyond $x = \delta$ along with the temperature decay. In the initial region of the jet, around $x < 5\delta$, radiative heat transfer is dominated by emission power, yet the absorption is around 61% of the emitted power at $x = 5\delta$. As the flow evolves downstream, the difference between emitted and absorbed power decreases. Then, beyond $x > 9\delta$, in the fully developed region, absorption is around 80% of the emitted power. **The downstream evolution of the optical thickness is depicted by the spectral transmissivity shown in Fig. 12. Similarly to Fig. 3, the spectral transmissivity is defined from an isothermal and homogeneous water vapor column of length l = 0.05 m (initial jet width) and pressure of 2.576 atm. Here, the jet centerline's local temperature is considered to account for the evolution of the transmissivity at the axial coordinate.** Since the optical thickness does not vary significantly downstream, the strong absorption observed beyond $x > 9\delta$ at the jet centerline is because of considerable reabsorption, i.e., most of the emitted energy is reabsorbed near the emission point; but also because there is, in some extend, absorption from a large amount of radiation emitted

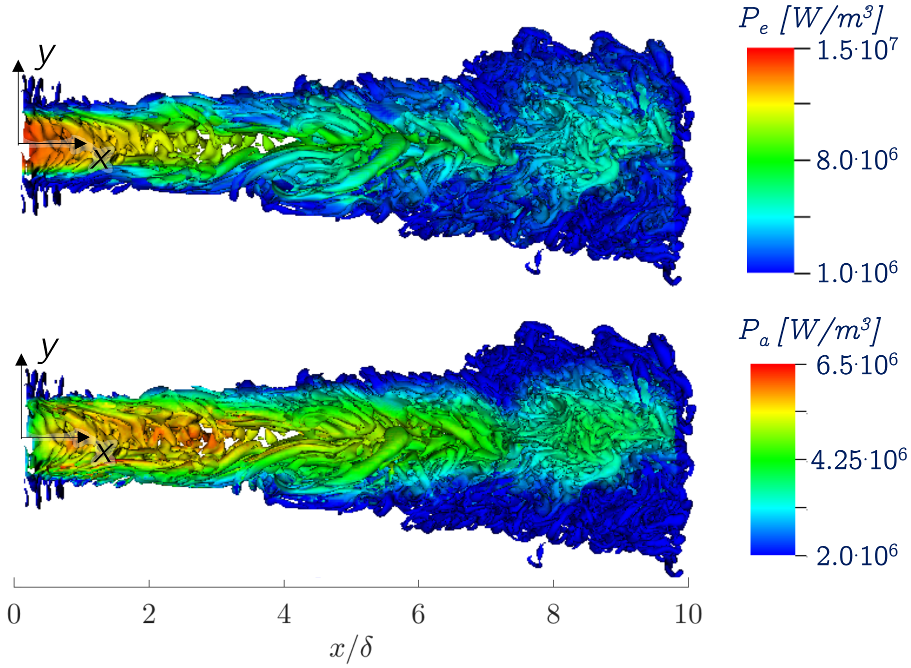

Figure 9: Snapshots of turbulent eddies identified by the Q-criterion colored by P_e and P_a.

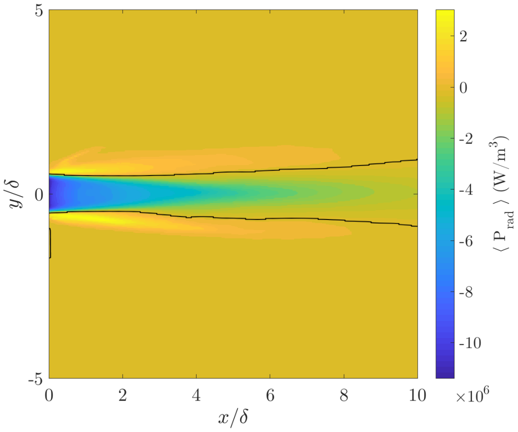

Figure 10: Contour of the mean radiative power of the strongly heated jet. A solid black line delimits the emission dominated region from the absorption dominated region.

at the inlet region. The nature of this energy exchange has not been fully characterized in this work, which would require further information regarding the ray paths.

The mean radiative power along the jet centerline, resulting from the difference between the mean emission and mean absorption radiative powers, is presented in Fig. 11b. The initial zone is the most affected region by radiation due to the large radiative power emitted. Then, radiative power at the jet centerline tends to zero downstream as the turbulent jet spreads and mixes itself with its surrounding.

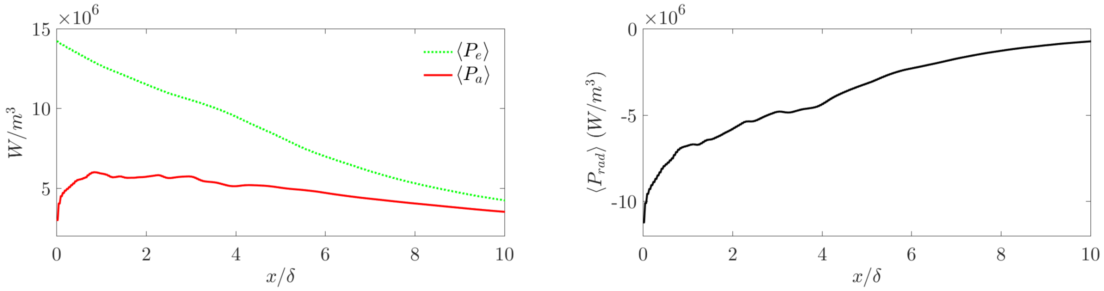

(a) (b)

Figure 11: Downstream evolution along the jet centerline of (a) $\langle P_a \rangle$ and $\langle P_e \rangle$, and (b) $\langle P_{rad} \rangle$.

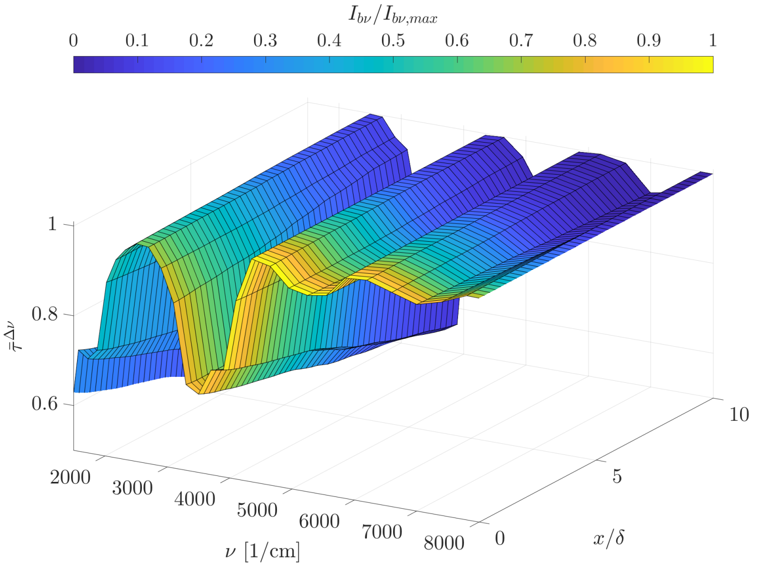

Figure 12: Spectral transmissivity of water vapor based on the initial jet width length and the temperature downstream evolution at the jet centerline colored by the spectral Planck function adimensionalized by its maximum value.

The cross-section profiles of mean emission and mean radiative absorption powers in the initial zone ($x = \delta$) are shown in Fig. 13a. A maximum relative difference of around 53% between the emitted and the absorption powers at the jet centerline is observed. The resulting mean radiative power at $x = \delta$ is presented in Fig. 13b. Figure 13b shows a strong emitted radiative power in the jet potential core. On the jet edges, the radiative power tends to zero, and absorption dominates in the outer region of the jet. In the fully developed zone, the temperature and its gradients are lower, and the heat transport by radiation decreases significantly. This considerable reduction of the radiative power at $x = 10\delta$ is illustrated in Fig. 13c, which shows that the relative difference between mean emission and absorption powers is around 17%. These values are reflected in the mean radiative power cross-section at $x = 10\delta$ presented in Fig. 13d.

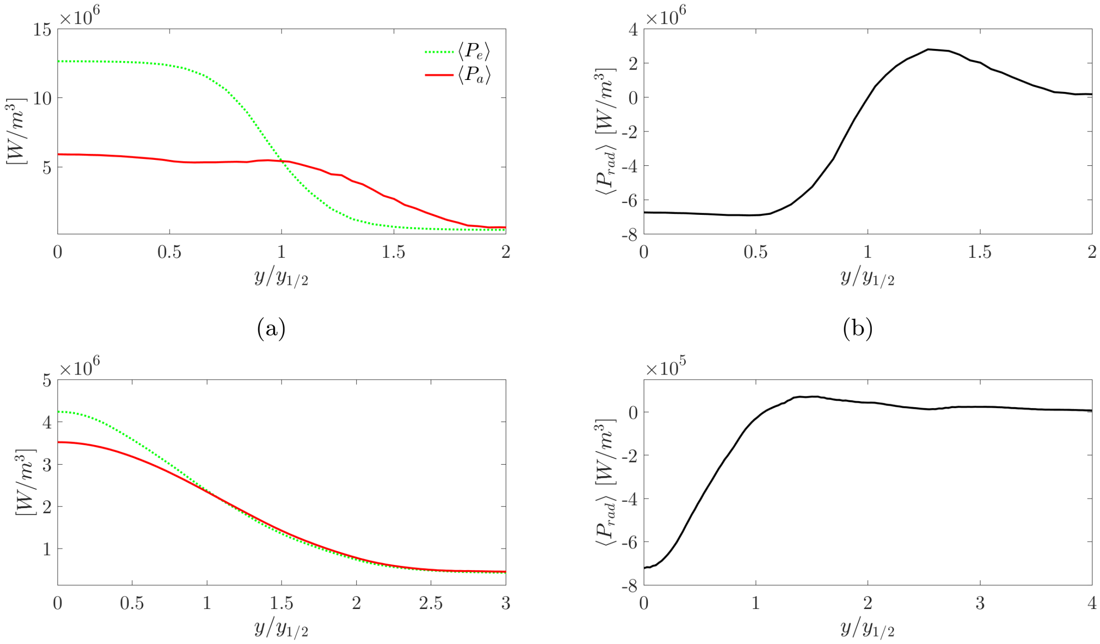

(a) (b)

(c) (d)

Figure 13: Cross-section profiles of mean emission, mean absorption and mean radiative powers at the initial ($x = \delta$) and fully developed ($x = 10\delta$) regions. (a) $\langle P_a \rangle$ and $\langle P_e \rangle$ at $x = \delta$, (b) $\langle P_{rad} \rangle$ profile at $x = \delta$, (c) $\langle P_a \rangle$ and $\langle P_e \rangle$ at $x = 10\delta$, and (d) $\langle P_{rad} \rangle$ profile at $x = 10\delta$.

Although the mean radiative power decreases significantly downstream, its cross-section profiles have similar trends in the downstream region. **An** adimensionalization is proposed to characterize the cross-section profiles of mean radiative power in the fully developed turbulent region. The adimensionalization is based on the distance from the centerline of the jet at which the mean radiative power is null $y_{1/2,P_{rad}}(x)$ and the magnitude of mean radiative power at the jet centerline $\langle P_{c,rad} \rangle$. On the one hand, Fig. 14a shows how dimensional radiative power profiles versus the cross-stream coordinate adimensionalized by the half-width based on velocity do not collapse into the same profile and how they decrease in magnitude downstream. On the other hand, Fig. 14b shows the adimensionalized radiative power profiles at $x = 8\delta$, $x = 9\delta$ and $x = 10\delta$. This adimensionalization induces reasonable self-similar profiles of mean radiative power beyond $x = 8\delta$. A reason for the observed self-similarity in the radiative power would be due to self-similarity in the temperature profiles in addition to strong reabsorption such that local conditions determine the radiative power.

The qualitative behavior of the radiative power shown in Fig. 10 is similar to the one in Ref. [33] for a slightly heated jet, and has been here thoroughly detailed. The first objective of the present study is to consider conditions under which the temperature profile is impacted by thermal radiation in the developed region of the jet. This requirement is verified in the next section.

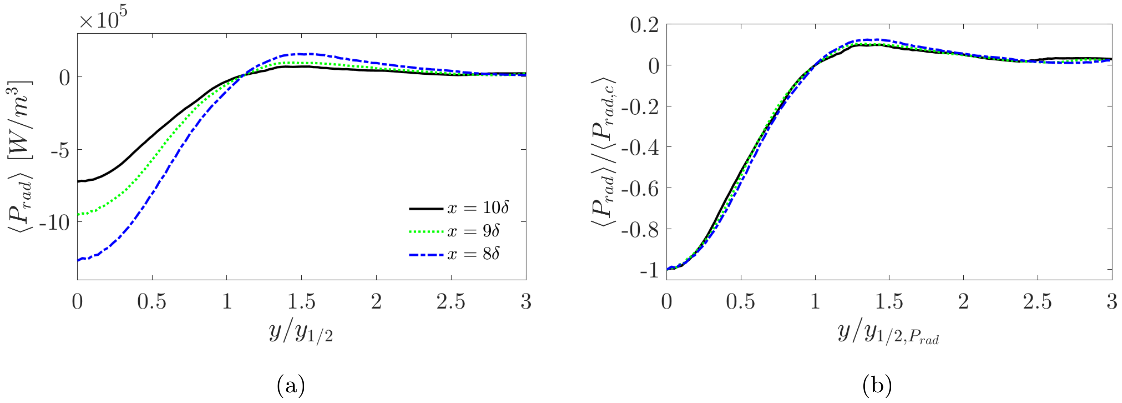

Figure 14: Adimensionalized radiative power profiles at different cross-sections.

4.2. Radiation effects on the mean temperature field

When accounting for radiation in the energy transport, the instantaneous temperature fields are significantly modified, as shown in Fig. 15. Despite there is not a clear difference in the turbulent structures identified by the Q-criterion, it can be seen qualitatively that the energy mixing process is enhanced by the presence of thermal radiation. **Note that, although the injected hot mixture remains uniform in terms of temperature at the vicinity of the nozzle, early turbulent structures in this region can be identified in Fig. 15 due to the injected synthetic turbulence at the inlet.** Plots analyzing velocity fields are not presented. To summarize briefly, first-order moments are moderately impacted by the impact of radiation through density variations. As for second-order moments or terms in the budget of kinetic energy, the effect of radiation is negligible on adimensionalized profiles.

On the other hand, temperature statistics are, of course, greatly affected by thermal radiation. The mean temperature fields are shown in Fig. 16. Radiation enhances the energy transport, especially in the entrance zone at which high temperature and large temperature gradients are present as already observed in slightly heated conditions [33]. It can be seen in Fig. 16 that radiation shortens the temperature potential core and smooths the gradients of mean temperature.

Figure 17 shows the jet half-width based on temperature $y_{1/2,T}$ adimensionalized by the initial jet width δ for the radiative and the non-radiative cases. From this figure, it can be observed that the jet starts spreading beyond $x = 3\delta$ when radiation is included. On the other hand, for the non-radiative jet, the jet starts spreading afterward around $x = 5\delta$. Such a difference is caused by the enhanced energy transport when including radiation effects.

The radiation role in heat transport is assessed through the average enthalpy balance. For a

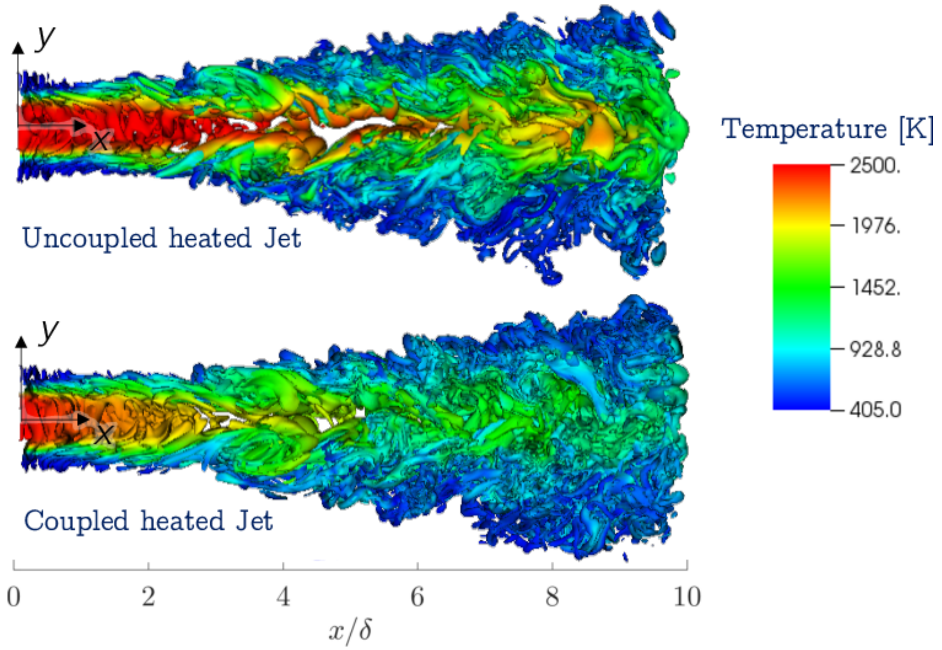

Figure 15: Snapshots of turbulent eddies identified by the Q-criterion colored by temperature for the heated jet without including radiation, and the heated jet coupled with the radiative solver.

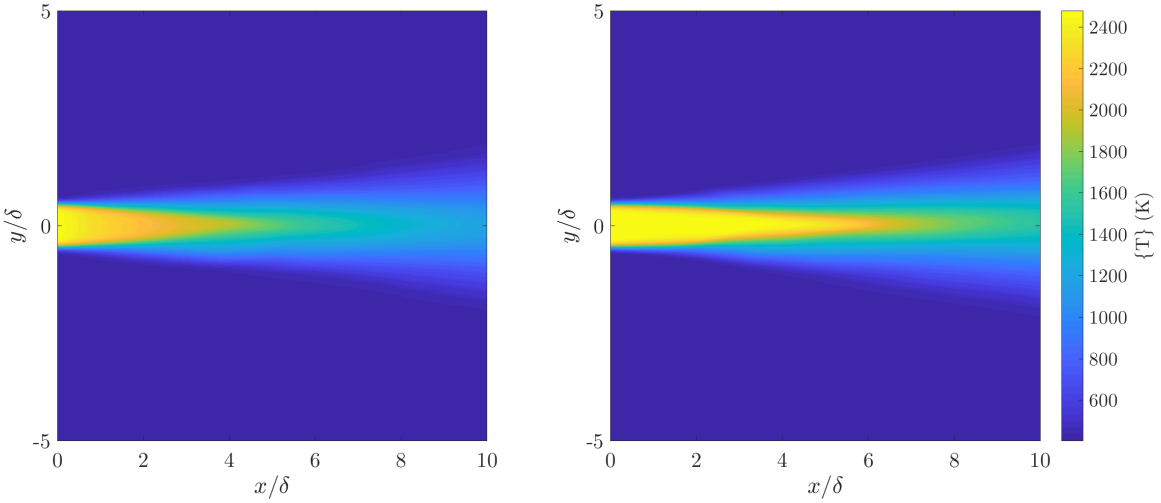

(a) (b)

Figure 16: Comparison of Favre-averaged temperature fields between (a) the radiative and the (b) non-radiative heated plane jets.

statistically steady-state and a low Mach-number flow, it can be written as

$$\underbrace{\frac{\partial\left(\langle\rho\rangle\{u_i\}\{h\}\right)}{\partial x_i}}_{\text{Mean flow advection}} + \underbrace{\frac{\partial\left(\langle\rho\rangle\{u_i''h''\}\right)}{\partial x_i}}_{\text{Turbulent convective heat flux}} = \underbrace{\frac{\partial}{\partial x_i}\left\langle\lambda\frac{\partial T}{\partial x_i}\right\rangle}_{\text{Molecular diffusion}} + \underbrace{\langle P_{rad}\rangle}_{\text{Radiative power}}. \tag{10}$$

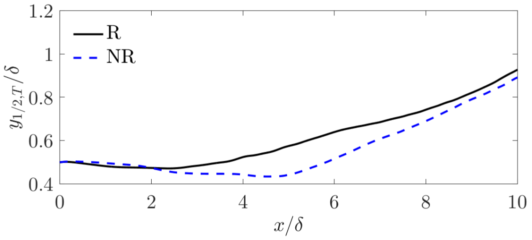

Figure 17: Downstream evolution of the jet half-width based on temperature profile for the radiative and non-radiative jets.

Figure 18 presents the cross-section profiles of the terms in Eq. (10) in the initial region ($x = \delta$) adimensionalized by the factor $y_{1/2}/\left(\Delta\{U_c\}C_p\Delta\{T_c\}\langle\rho\rangle\right)$ for the uncoupled (Fig. 18a) and the coupled (Fig. 18b) simulations, in which $\Delta\{T_c\} = \{T\}_{y=0} - T_2$. As expected, Figure 18b shows that radiation has a major contribution in the initial zone, specially in the inner region of the jet as seen in [33]. Note that the radiation contribution to the enthalpy budget at jet inner region is compensated by the mean flow advection.

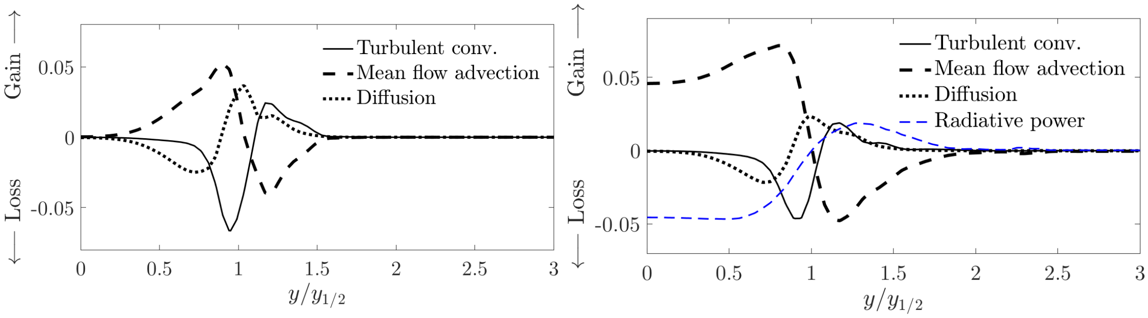

(a)

(b)

Figure 18: Cross-section profiles of the enthalpy budget main terms at $x = \delta$ for (a) the non-radiative and (b) the radiative jets.

Figure 19 shows the same analysis in the developed region. Again, all terms of the balance have been adimensionalized by the factor $y_{1/2}/\left(\Delta\{U_c\}C_p\Delta\{T_c\}\langle\rho\rangle\right)$. Despite the drop in thermal radiative power in the downstream region, radiation keeps, under the studied conditions, a noticeable contribution to the enthalpy balance for $y < y_{1/2}$ in the developed region as shown in Fig. 19b. This behavior is different from the previously studied conditions in [33] and corresponds to the desired physical conditions for the present study.

As explained in [33], thermal radiation can have two kinds of effects on the temperature profile in the developed region: a direct one from radiative energy transfer and an indirect one due to the modified flow density issued from the perturbed initial zone. The presence of the direct effect in the

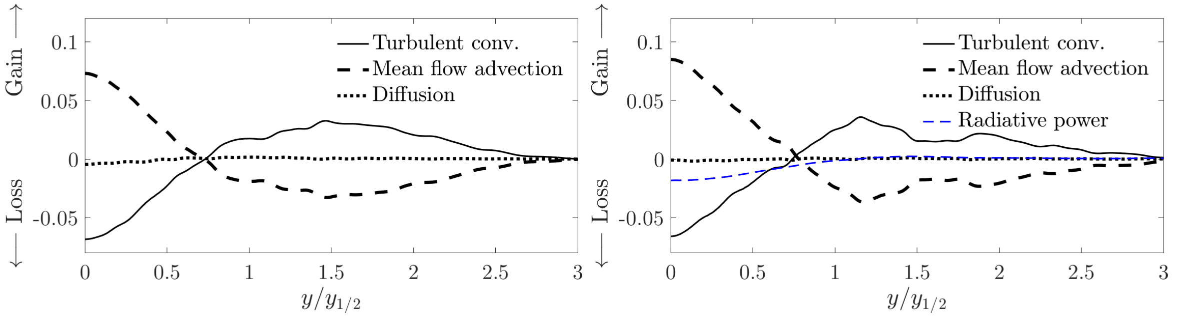

(a)

(b)

Figure 19: Cross-section profiles of the enthalpy budget main terms at $x = 10\delta$ for (a) the non-radiative and (b) the radiative jets.

developed region can be additionally confirmed with the scaling derived for the temperature decay in [33]. A classical plot based on $\Delta\{T_c\} = \{T\}_{y=0} - T_2$ and $\Delta T_0 = T_1 - T_2$ to show the temperature decay at the jet centerline is presented in Fig. 20a. The temperature decay is faster for the radiative case (R) than for the non-radiative case (NR), in particular in the developed region. This information can, however, be dubious on the importance of radiation in this region as outlined in [33] and could be the sole result of the previously described indirect effect. In the work of [33], a new scaling has been derived to correct for variable-density effects associated to this indirect effect. In Figure 20b, the streamwise coordinate is now scaled based on an equivalent heat jet opening ($r_{\epsilon,T}$) defined in [33] as

$$r_{\epsilon,T} = \frac{\delta^2}{y_{1/2,T}} \left(\frac{\overline{\rho_0}}{\langle \rho_c \rangle}\right)^2 \left(\frac{\overline{u_0}}{\{U_c\}}\right)^2, \tag{11}$$

where the exit nozzle density ($\overline{\rho_0}$) and velocity ($\overline{u_0}$) are considered as the bulk average defined as $\overline{\rho_0} = \frac{1}{\delta}\int_\delta \rho_{|x=0} dy$ and $\overline{u_0} = \frac{1}{\delta}\int_\delta U_{in}(y) dy$, respectively.

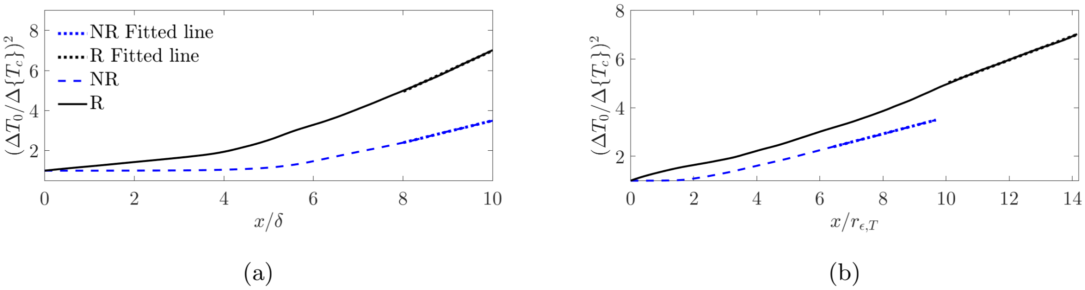

(a)

(b)

Figure 20: Downstream temperature decay along the present heated jet centerline for the radiative (R) and non-radiative (NR) jets using (a) classical scaling (b) scaling from [33].

Results for the new scaling in Fig. 20b for both simulations show two curves that remain different contrary to results for a slightly heated jet in [33] where only the indirect effect explained the temperature profile in the developed region. This difference indicates and confirms the role of the direct effect of thermal radiation in the present jet developed region.

Linear fitting of the form

$$\left(\frac{\Delta T_0}{\Delta\{T_c\}}\right)^2 = Q_{1,T}\left(\frac{x}{r_{\epsilon,T}} + Q_{2,T}\right), \tag{12}$$

is additionally included in Fig. 20 for both cases to quantify the decay rates. Results of the linear coefficients using both the classical and the new scaling are presented in Table 2 . With the appropriate new scaling, the temperature decay rate $Q_{1,T}$ is indeed different between the radiative and the non-radiative cases, with a relative difference of 30.4 %. This analysis is in accordance with the average enthalpy balance in the developed region presented in Fig. 19b, which states that the nature of the heat transfer is modified by the inclusion of radiation.

Table 2: Comparison of decay and spread of temperature fitted coefficients for the radiative and non-radiative heated jets using scaling based on the convective heat flux conservation.

Scaling	Jet case	$Q_{1,T}$	$Q_{2,T}$
Classic scaling	Non-radiative	0.552	-3.650
	Radiative	1.022	-3.218
New scaling	Non-radiative	0.3386	0.645
	Radiative	0.4867	0.251

Finally, excess Favre averaged temperature profiles ($\{T_e\} = \{T\} - T_2$) of the radiative and the non-radiative jets are presented in Fig. 21 adimensionalized by $\Delta\{T_c\}$ at $x = 10\delta$ and plotted against $y/y_{1/2,T}$. When adimensionalized, temperature profiles of the radiative and non-radiative cases are surprisingly very similar. This self-similarity was anticipated in the analysis of the radiative power profiles in §4.1.

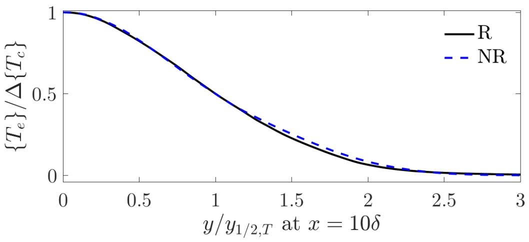

Figure 21: Comparison of cross-section profiles of mean excess temperature adimensionalized by the mean excess centerline temperature at $x = 10\delta$ for the radiative and non-radiative jets.

4.3. Radiation effects on temperature fluctuations

The relative magnitude of turbulent temperature fluctuations is presented in Fig. 22 by normalizing the temperature root-mean-square by the local mean temperature. Although a similar pattern is obtained when including radiative heat transfer, thermal radiation appears to slightly decrease temperature fluctuations, as observed by several previous studies such as [8, 29].

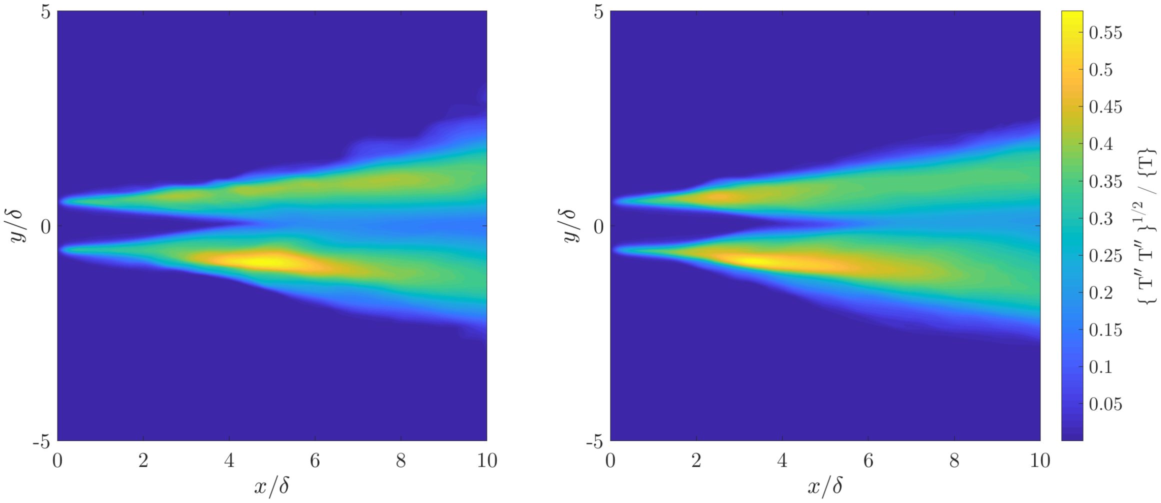

(a) (b)

Figure 22: Comparison of temperature root-mean-square between (a) the radiative and the (b) non-radiative jets.

Figure 23a shows the temperature root-mean-square along the jet centerline adimensionalized by the excess temperature $\Delta\{T_c\}$. For both cases, temperature fluctuations start to develop beyond $x = 3.5\delta$. However, in the radiative case, temperature fluctuations intensity remains lower than in the non-radiative jet. At the developed region ($x > 8\delta$), radiation decreases the temperature fluctuations around 38 % in the jet centerline. The dimensionless cross-section profiles of temperature fluctuations at $x = 10\delta$ are presented in Fig. 23b. In accordance with Fig. 23a, temperature fluctuations at the jet centerline are lower for the radiative jet. However, temperature fluctuations are almost equal on both cases beyond $y = 1.2y_{1/2}$ at the developed zone when adimensionalized by $\Delta\{T_c\}$.

The effect of radiation on temperature fluctuations is further analyzed through the transport equation of Favre averaged enthalpy variance, $\Theta = \frac{1}{2}\{h''^2\}$. Following the development in the work of [29],

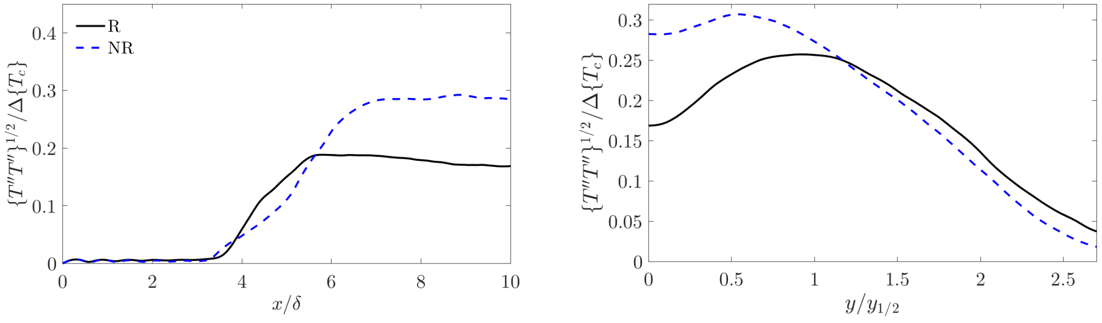

(a) (b)

Figure 23: Comparison of temperature root-mean-square profils between the radiative and the non-radiative jets. (a) Downstream evolution along the jet centerline. (b) Cross-section profile at $x = 10\delta$.

for a low-Mach flow, the enthalpy variance transport equation can be expressed as:

$$\begin{aligned}\underbrace{\frac{1}{2}\frac{\partial}{\partial t}\left(\langle\rho\rangle\{h''^2\}\right)+\frac{\partial}{\partial x_j}\left(\frac{1}{2}\langle\rho\rangle\{u_j\}\{h''^2\}\right)}_{\text{Advection, }\langle\rho\rangle\frac{\bar{D}\Theta}{\bar{D}t}} &= -\underbrace{\frac{\partial\langle q_j'h'\rangle}{\partial x_j}}_{\text{Molecular diffusion },\ \mathcal{D}_\Theta} \\ &+ \underbrace{\left\langle q_j'\frac{\partial h'}{\partial x_j}\right\rangle}_{\text{Molecular dissipation, }\epsilon_\Theta} - \underbrace{\langle\rho\rangle\{u_j''h''\}\frac{\partial\{h\}}{\partial x_j}}_{\text{Production, }\mathcal{P}_\Theta} - \underbrace{\frac{\partial}{\partial x_j}\langle\rho\rangle\{u_j''\frac{h''^2}{2}\}}_{\text{Turbulent difusion, }\nabla\cdot T'_\Theta} \\ &- \underbrace{\langle h''\rangle\frac{\partial\langle q_j\rangle}{\partial x_j}}_{\text{I}} + \underbrace{\langle h''\rangle\langle P_{rad}\rangle}_{\text{II}} + \underbrace{\langle h''P'_{rad}\rangle}_{\text{III}}\end{aligned} \tag{13}$$

The molecular diffusion and Terms I and II are neglected in the following analysis since they do not contribute significantly in the present enthalpy fluctuations balance. Then, adimensionalizing all terms in the enthalpy fluctuations budget by the factor $\frac{y_{1/2}}{\Delta U_c(C_p\Delta T_c)^2\langle\rho\rangle}$, Eq. 13 can be rewritten as

$$\frac{\bar{D}\Theta}{\bar{D}t}^{*} = \epsilon_\Theta^* + \mathcal{P}_\Theta^* + \nabla\cdot T_\Theta'^* + \langle h''P'_{rad}\rangle^* \tag{14}$$

where * denotes adimensionalized quantities.

The budget of the enthalpy fluctuations for the non-radiative and radiative jets are presented in Figs. 24a and 24b, respectively. As expected, in the non-radiative jet, production and dissipation terms dominate the budget. However, when radiation is included, a new term corresponding to the correlation between enthalpy fluctuations and radiative power fluctuations significantly contributes to an additional dissipation mechanism of enthalpy variance. That is why we called this term radiative dissipation as in the work of [29]. Although the unbalance terms remain quite small in both budgets, it must be said that, for the radiative case, the budget is not completely close. This residual error may be attributed to numerical dissipation introduced in the resolution of the RTE on a coarser mesh.

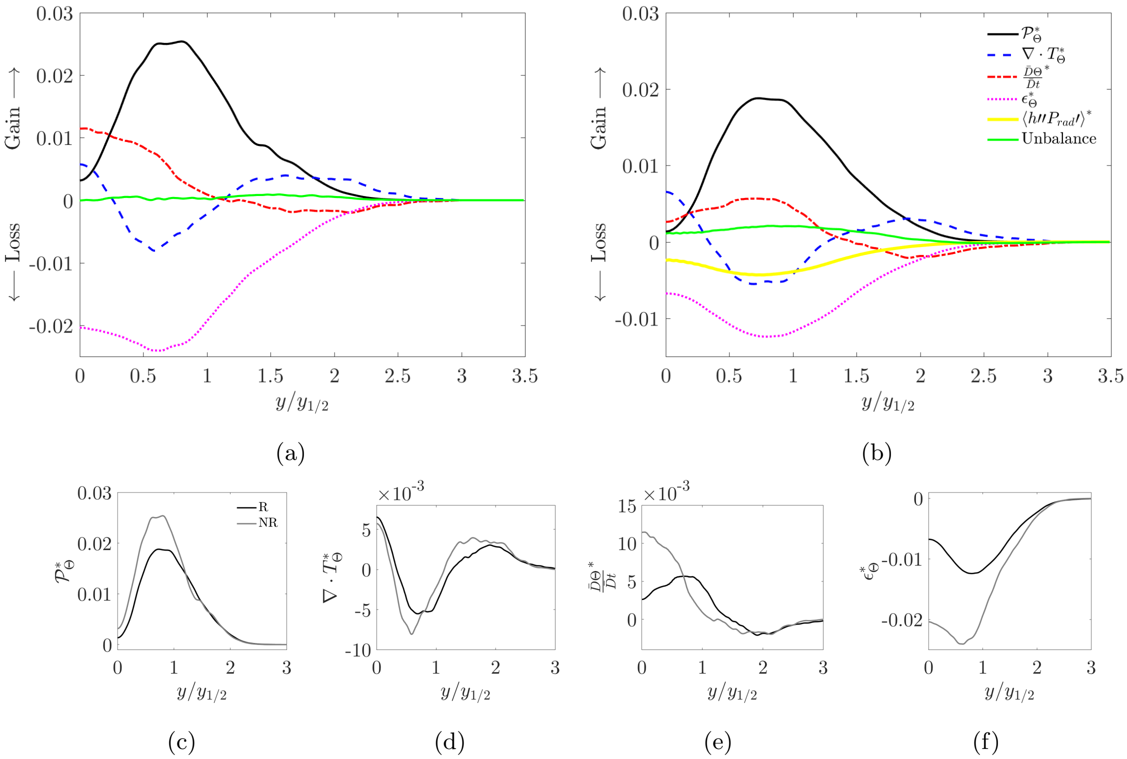

Figure 24: Dimensionless budget of enthalpy variance in the developed region. (a) Uncoupled heated jet. (b) Accounting for radiative heat transfer. Comparison of the contributions in the enthalpy variance budget: (c) production, (d) turbulent diffusion, (e) advection and (f) molecular dissipation between the radiative and the non-radiative jet cases.

The negative sign of term III outlines the anti-correlation between h'' and P'_{rad}: an increase in local temperature yields a negative variation in the radiative power. This term, previously identified in wall-bounded flows [26, 29], is also responsible in the present free shear flow for an additional damping mechanism of temperature fluctuations.

A comparison of each term in the balance between both cases is presented in Figs. 24c to 24f. When radiation is taken into account, the production term decreases because the mean temperature gradients $\left(\dfrac{\partial \{h\}}{\partial x_j}\right)$ have been smoothed by thermal radiation, and the decrease in temperature fluctuations certainly weakens the turbulent transport $(-\langle \rho \rangle \{u_j'' h''\})$. Reciprocally, due to the decrease in production and the additional radiative dissipation mechanism, the enthalpy variance in Fig. 23 decreases: there is a complex equilibrium between the mean fields, their fluctuations, and the effect of radiation on both. Then, because of the acting radiative dissipation mechanism and the decreased enthalpy variance, the molecular dissipative term nearly decreases by a factor of two when radiation is considered.

4.4. Radiation effects on the temperature spectrum

To complete the analysis of radiation effects on second-order moments of temperature, the spectrum of temperature fluctuations at $x = 10\delta$ and at the jet centerline ($y = 0$) is presented in Fig. 25 to analyze how the different turbulent eddies are affected by radiation. The spectrum $E_T(\mathcal{K}_z)$ is computed along the homogeneous spanwise direction for the radiative and non-radiative cases. Both spectra are first scaled by the large turbulent motions using the jet half-width $y_{1/2}$ and the mean excess centerline temperature $\Delta\{T_c\}$. The classical representation of the one-dimensional spectra based on a single wavenumber direction is shown in Fig. 25a. **This figure shows that the flow at the developed region presents a wide range of length scales, producing a continuous and smooth spectrum characteristic of fully turbulent flows.** Such a description, however, cannot identify energetic eddies: no peak is seen as the wavenumber $\mathcal{K}_z$ does not account for the eddies extent in other directions. The premultiplied one-dimensional spectrum ($\mathcal{K}_x E_T$), described in the work of Alamo *et al.* [50, 51], allows for correcting this shortcoming. It is presented in Fig. 25b which expresses the premultiplied spectra as functions of the wavelength ($\frac{2\pi}{\mathcal{K}_x}$) to identify the most energetic regions. With the previously described drop in temperature variance, the L2-norm of the spectrum with radiation is expected to be smaller than the case without it. From both Figures 25a and 25b, it can be observed that radiation indeed decreases the intensity of fluctuations, and that is, in fact, true at all scales. However, when these profiles are scaled by their respective temperature variances, radiative and non-radiative spectra have very similar trends, as shown in Fig. 26. The inertial region is almost superposed for the radiative and non-radiative cases, while slight differences can be observed in the dissipative and the energy-containing ranges.

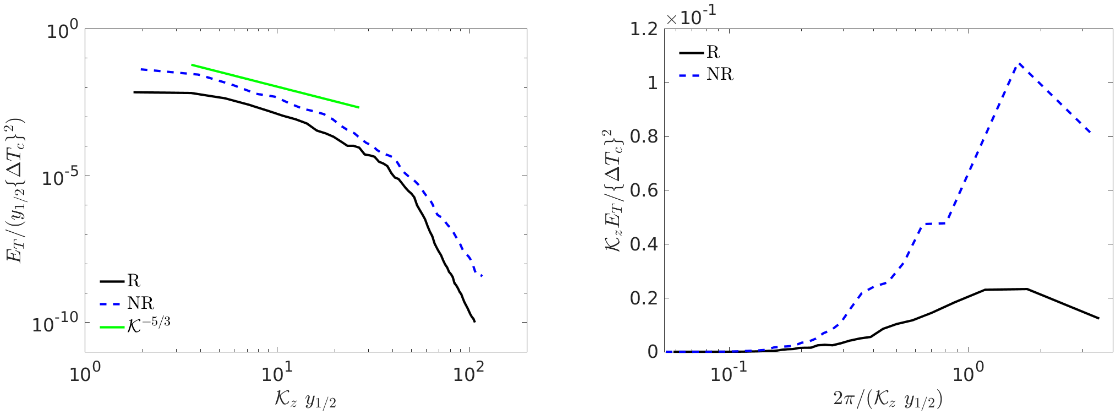

(a) (b)

Figure 25: One-dimensional spectra of temperature fluctuations along the homogeneous spanwise direction at the jet centerline and at $x = 10\delta$ for the radiative (R) and non-radiative (NR) jets. (a) Classical representation of the one-dimensional spectrum, (b) premultiplied one-dimensional spectrum.

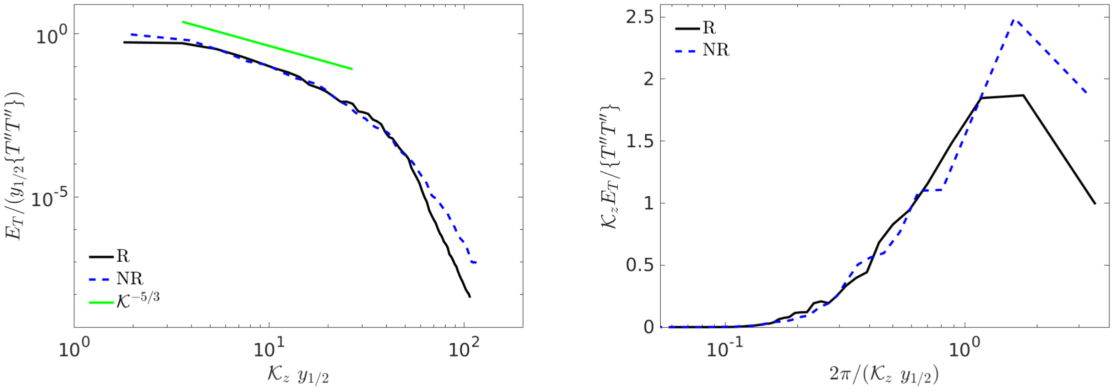

(a)

(b)

Figure 26: One-dimensional spectra of temperature fluctuations along the homogeneous spanwise direction at the jet centerline and at $x = 10\delta$ for the radiative (R) and non-radiative (NR) jets scaled by temperature fluctuations. (a) Classical representation of the one-dimensional spectrum, (b) premultiplied one-dimensional spectrum.

To further understand the role of radiation on the temperature fluctuations spectrum, Figure 27a compares the premultiplied one-dimensional spectrum of the radiative dissipation $\langle h'' P'_{rad} \rangle$ denoted by $\mathcal{D}_{P_{rad}}$ with the premultiplied molecular dissipation spectra related to the term $\left\langle \frac{\partial h'}{\partial z} \frac{\partial h'}{\partial z} \right\rangle$ designated by $\mathcal{D}_{\epsilon,R}$ and $\mathcal{D}_{\epsilon,NR}$ for the radiative and non-radiative cases, respectively. Radiation dissipation acts mainly in large turbulent scales, while, as expected, the molecular dissipation process occurs in small eddies. Moreover, radiative dissipation can be split into emission and absorption contributions as $\langle h'' P'_{rad} \rangle = \langle h'' P'_{a} \rangle - \langle h'' P'_{e} \rangle$. Figure 27b shows the premultiplied spectra associated to $\langle h'' P'_{e} \rangle$ and $\langle h'' P'_{a} \rangle$ denoted as $\mathcal{D}_{P_e}$ and $\mathcal{D}_{P_a}$, respectively, together with the already seen spectra for temperature fluctuation and radiative dissipation. From Fig. 27b, it can be seen that radiative dissipation associated to the emitted power controls the total radiative dissipation at the jet centerline, while the contribution associated to the absorption part is small. Since emission dominates in the centerline of the jet as presented in Fig. 10, a strong correlation between temperature and radiative power is expected; thus, radiative dissipation and temperature fluctuations spectra have very similar trends.

4.5. Turbulent Prandtl number

Since radiation decreases mean temperature gradients and also affects second-order temperature moments, as shown above, the Turbulent Prandtl number (Pr_t) is therefore subject to change due to radiation effects. Pr_t is typically a calibrated parameter in the context of turbulent viscosity models, in which the turbulent heat flux is commonly related to the mean flow characteristics by the expression

$$\langle \rho \rangle \{u''_j T''\} = -\frac{\mu_t}{\mathrm{Pr}_t} \frac{\partial \{T\}}{\partial x_j}, \tag{15}$$

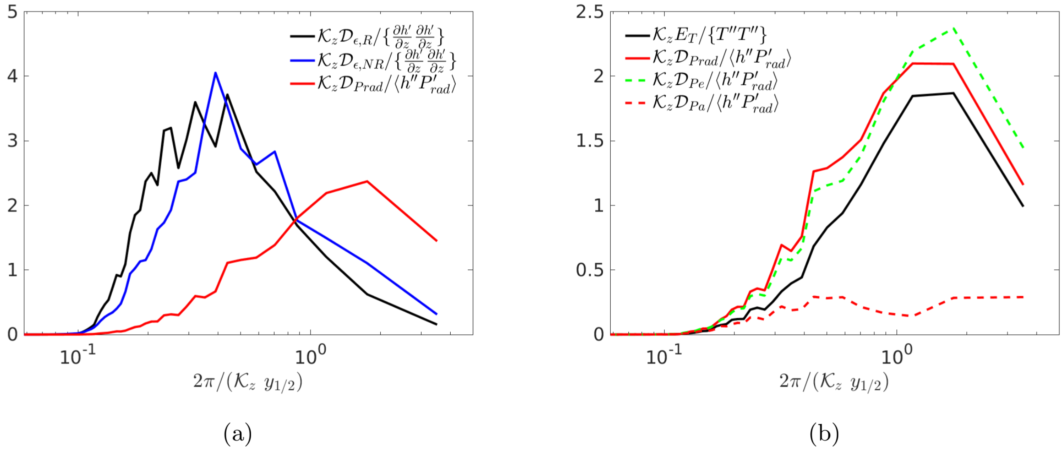

(a)

(b)

Figure 27: Premultiplied one-dimensional spectra (at $x = 10\delta$ and $y = 0$) along the homogeneous spanwise direction. (a) Radiative and molecular dissipation spectra for the radiative (R) and non-radiative (NR) jets. (b) Comparison betweeen the radiative dissipation spectra with its emission and absorption contributions, together with the spectra of temperature fluctuations for the radiative case.

475 where μ_t is the so-called turbulent viscosity. In order to assess the radiation effects on Pr_t, it has been explicitly computed for the radiative and the **non-radiative** cases using the following expression, valid in thin layers,

$$\mathrm{Pr}_t = \frac{-\langle\rho\rangle\{u''v''\}}{-\langle\rho\rangle\{v''h''\}/cp} \frac{\partial\{T\}/\partial y}{\partial\{u\}/\partial y}. \tag{16}$$

In Figures 28a to 28c the downstream evolution of Pr_t is plotted for three constant $y_{1/2}$-lines that are $y = y_{1/2}/2$, $y = y_{1/2}$ and $y = 3y_{1/2}/2$. While close to the jet centerline (Fig. 28a), the turbulent 480 Prandtl number is slightly greater for the NR case; as the distance to the jet centerline increases (Figs. 28b and 28c), the R case has larger Pr_t values when compared to the NR case.

In order to synthesize the increase in the turbulent Prandtl number due to radiation, the spatial averages of Pr_t computed in the range $5\delta < x < 10\delta$ for the iso-$y_{1/2}$-lines are reported in Table 3. At the outer region of the jet, the turbulent Prandtl number indeed increases due to the radiation 485 effects. The work of [29] in wall-bounded flows always revealed an increment of Pr_t when considering radiation. The behavior in a turbulent jet appears more sophisticated.

Table 3: Turbulent Prandtl number spatially averaged along lines of equal $y_{1/2}$ for the Radiative (R) and the Non-radiative (NR) cases of the strongly heated jet.

Case	$\overline{\mathrm{Pr}_t}$ at $y_{1/2}/2$	$\overline{\mathrm{Pr}_t}$ at $y_{1/2}$	$\overline{\mathrm{Pr}_t}$ at $3y_{1/2}/2$
R	0.5613	0.8249	1.1006
NR	0.7779	0.8811	0.8848

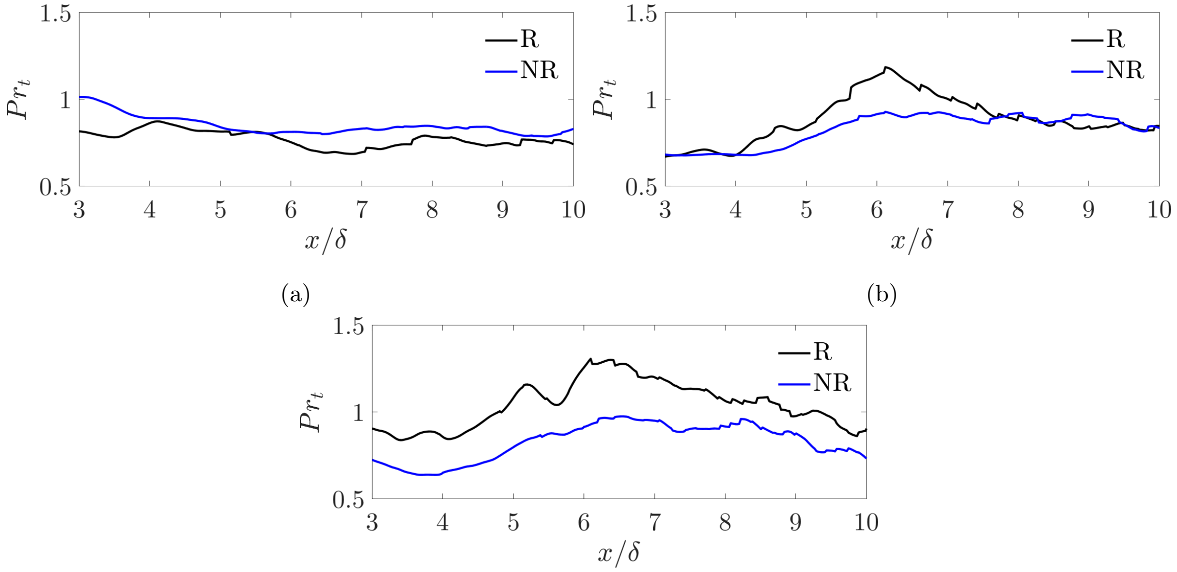

(a)

(b)

(c)

Figure 28: Comparison of Pr_t results between the radiative (R) and non-radiative (NR) cases along three different lines of equal $y_{1/2}$: (a) $y = y_{1/2}/2$, (b) $y = y_{1/2}$ and (c) $y = 3y_{1/2}/2$.

4.6. Interaction between radiative transfer and temperature turbulent fluctuations

The analysis of the turbulence effects on mean radiation is presented in this section. These effects arise due to radiation nonlinearities. Hence, the averaged radiation heat transfer in a fluctuating temperature field may differ from the one obtained using only the averaged temperature. To quantify the turbulence effects on radiation in the present configuration, a non-coupled Monte-Carlo computation of the radiative heat transfer using the averaged temperature field, $P_{rad}\left(\langle T\rangle\right)$, is compared with the averaged radiative power from the coupled simulation $\langle P_{rad}\left(T\right)\rangle$ presented in §4.1.

The downstream evolution of $P_{rad}\left(\langle T\rangle\right)$ and $\langle P_{rad}\left(T\right)\rangle$ at the jet centerline is presented in Fig. 29a, while, in Fig. 29b, a comparison between cross-section profiles of $P_{rad}\left(\langle T\rangle\right)$ and $\langle P_{rad}\left(T\right)\rangle$ at $x = 10\delta$ is shown. From Fig. 29, it can be observed that turbulence effects on the radiative power at the emission dominated jet centerline are very small: they do not exceed a relative difference of 10%. However, turbulence effects on the cross-section profile of radiative power are noticeable despite remaining moderate all along the profile.

The observed negligible-to-small turbulent effects on the average radiation field for the present configuration are in agreement with the literature which stands that, for most non-reactive flows, such turbulence-radiation interaction effects are negligible [21, 28, 29, 52, 53]. However, one cannot reduce TRI effects to the analysis of $\langle P_{rad}\rangle$. The previous sections have indeed outlined several other interactions.

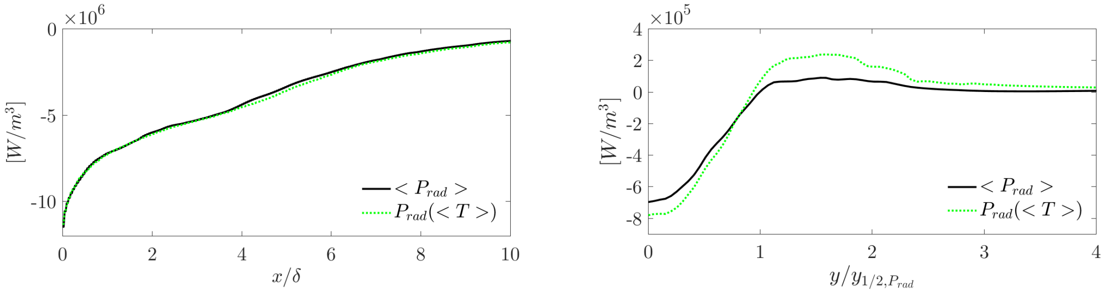

(a) (b)

Figure 29: Comparison between averaged radiative power field and radiative power from averaged temperature field. (a) Downstream evolution of $P_{rad}\left(\langle T\rangle\right)$ and $\langle P_{rad}\left(T\right)\rangle$ along the jet centerline and (b) Cross-section profile of $P_{rad}\left(\langle T\rangle\right)$ and $\langle P_{rad}\left(T\right)\rangle$ at $x = 10\delta$.

5. Conclusions

The impact of thermal radiation has been analyzed in a non-reactive turbulent jet with high-fidelity methods: direct numerical simulation, accurate radiative properties, and Monte Carlo radiative solver. Since coupling between solvers at each flow iteration and all computational nodes remains too costly, the impact of the numerical setup has first been investigated. The studied conditions magnify radiative heat transfer, which keeps a noticeable contribution in the jet developed region for $y < y_{1/2}$ in the enthalpy balance. The jet scaling law derived in [33] to account for variable-density effects in the jet temperature decay also confirms that a direct effect of radiation remains in this region. The case enables then to study the effect of radiation in the fully developed part of the considered free shear flow.

As in previous nonreactive studies, the effects of turbulence on the average radiative power are moderate. However, the reciprocal effects of radiation on the turbulent temperature scales exhibit a more sophisticated nature. The level of temperature fluctuations is damped in the presence of radiative heat transfer, which, in turn, affects the efficiency of the turbulent heat transfer. This results from two mechanisms: the thermal turbulent production is reduced, and a new dissipative term takes place because of the correlation term between local enthalpy and radiative power that appears in the budget. Under the studied configuration, this radiative dissipation contributes negatively to the temperature fluctuations and is dominated by its emission contribution. Finally, the turbulence spectrum analysis reveals that energetic eddies are responsible for this damping mechanism, which is very different from the classical molecular dissipation that takes place at the smallest eddies. As for the modified turbulent heat transport, the effects of radiation have eventually been synthesized in terms of its impact on turbulent Prandtl number from the DNS data. The behavior is not uniform throughout the jet cross-section: Pr_t decreases close to the jet centerline, while an increase is observed at the outer region.

A broad range of complexity in the effects of radiation on turbulent flows has been observed. Future works will be needed to understand if this prevails in other cases with intense thermal radiation and how the scaling laws are modified. Adimensionalization has shown self-similar profiles for mean temperature and radiative power, which is surprising given that detailed radiative properties leave little hope for universal profiles. Other cases would allow for assessing this feature. A longer extent for the studied jet (here prohibited by the available resources) would also be interested in observing whether a change in the balance between thermal radiation and turbulent heat transfer takes place further downstream.

Acknowledgments

The authors wish to thank CAPES (Brazilian Federal Agency for Support and Evaluation of Graduate Education within the Ministry of Education of Brazil) and Centrale Recherce S.A. for the financial support. This work was performed using HPC resources from the “Mésocentre” computing center of CentraleSupélec and École Normale Supérieure Paris-Saclay supported by CNRS and Région Île-de-France (http://mesocentre.centralesupelec.fr/).

References

[1] P. J. Coelho, Numerical simulation of the interaction between turbulence and radiation in reactive flows, Progress in Energy and Combustion Science 33 (4) (2007) 311–383.

[2] M. F. Modest, D. C. Haworth, Radiative Heat Transfer in Turbulent Combustion Systems: Theory and Applications, Springer, 2016.

[3] G. Faeth, J. Gore, S.-M. Jeng, Spectral and total radiation properties of turbulent carbon monoxide/air diffusion flames, AIAA journal 25 (2) (1987) 339–345.

[4] P. Coelho, Detailed numerical simulation of radiative transfer in a nonluminous turbulent jet diffusion flame, Combustion and flame 136 (4) (2004) 481–492.

[5] G. Li, M. F. Modest, Importance of turbulence-radiation interactions in turbulent diffusion jet flames, Journal of heat transfer 125 (5) (2003) 831–838.

[6] Y. Wu, D. Haworth, M. Modest, B. Cuenot, Direct numerical simulation of turbulence/radiation interaction in premixed combustion systems, Proceedings of the Combustion Institute 30 (1) (2005) 639–646.

[7] T. Song, R. Viskanta, Interaction of radiation with turbulence-application to a combustion system, Journal of thermophysics and heat transfer 1 (1) (1987) 56–62.

[8] L. Tessé, F. Dupoirieux, J. Taine, Monte carlo modeling of radiative transfer in a turbulent sooty flame, International journal of heat and mass transfer 47 (3) (2004) 555–572.

[9] D. Poitou, J. Amaya, M. El Hafi, B. Cuenot, Analysis of the interaction between turbulent combustion and thermal radiation using unsteady coupled les/dom simulations, Combustion and Flame 159 (4) (2012) 1605–1618.

[10] R. G. dos Santos, M. Lecanu, S. Ducruix, O. Gicquel, E. Iacona, D. Veynante, Coupled large eddy simulations of turbulent combustion and radiative heat transfer, Combustion and Flame 152 (3) (2008) 387–400.

[11] R. G. dos Santos, S. Ducruix, O. Gicquel, D. Veynate, A study of three-dimensional les of turbulent combustion with radiative heat transfer, Journal of the Brazilian Society of Mechanical Sciences and Engineering (2015) 1–16.

[12] S. Berger, S. Richard, F. Duchaine, G. Staffelbach, L. Gicquel, On the sensitivity of a helicopter combustor wall temperature to convective and radiative thermal loads, Applied Thermal Engineering 103 (2016) 1450–1459.

[13] C. Koren, R. Vicquelin, O. Gicquel, Multiphysics simulation combining large-eddy simulation, wall heat conduction and radiative energy transfer to predict wall temperature induced by a confined premixed swirling flame, Flow, Turbulence and Combustion 101 (1) (2018) 77–102.

[14] P. Rodrigues, O. Gicquel, B. Franzelli, N. Darabiha, R. Vicquelin, Analysis of radiative transfer in a turbulent sooting jet flame using a monte carlo method coupled to large eddy simulation, Journal of Quantitative Spectroscopy and Radiative Transfer 235 (2019) 187–203.

[15] F. Kritzstein, A. Soufiani, Infrared gas radiation from a homogeneously turbulent medium, International journal of heat and mass transfer 36 (7) (1993) 1749–1762.

[16] C. B. da Silva, I. Malico, P. J. Coelho, Radiation statistics in homogeneous isotropic turbulence, New Journal of Physics 11 (9) (2009) 093001.

[17] M. Roger, C. B. Da Silva, P. J. Coelho, Analysis of the turbulence–radiation interactions for large eddy simulations of turbulent flows, International Journal of Heat and Mass Transfer 52 (9-10) (2009) 2243–2254.

[18] M. Roger, P. J. Coelho, C. B. da Silva, The influence of the non-resolved scales of thermal radiation in large eddy simulation of turbulent flows: A fundamental study, International Journal of Heat and Mass Transfer 53 (13-14) (2010) 2897–2907.

[19] M. Roger, P. Coelho, C. Da Silva, Relevance of the subgrid-scales for large eddy simulations of turbulence–radiation interactions in a turbulent plane jet, Journal of Quantitative Spectroscopy and Radiative Transfer 112 (7) (2011) 1250–1256.

[20] S. Ghosh, R. Friedrich, Effects of radiative heat transfer on the turbulence structure in inert and reacting mixing layers, Physics of Fluids 27 (5) (2015) 055107.

[21] A. Gupta, M. F. Modest, D. C. Haworth, Large-eddy simulation of turbulence-radiation interactions in a turbulent planar channel flow, Journal of Heat Transfer 131 (6) (2009) 061704.

[22] S. Ghosh, R. Friedrich, M. Pfitzner, C. Stemmer, B. Cuenot, M. El Hafi, Effects of radiative heat transfer on the structure of turbulent supersonic channel flow, Journal of Fluid Mechanics 677 (2011) 417–444.

[23] Y. Wu, M. F. Modest, D. C. Haworth, A high-order photon monte carlo method for radiative transfer in direct numerical simulation, Journal of Computational Physics 223 (2) (2007) 898–922.

[24] K. Deshmukh, M. Modest, D. Haworth, Direct numerical simulation of turbulence–radiation interactions in a statistically one-dimensional nonpremixed system, Journal of Quantitative spectroscopy and Radiative transfer 109 (14) (2008) 2391–2400.

[25] K. V. Deshmukh, D. C. Haworth, Higher-order spherical harmonics to model radiation in direct numerical simulation of turbulent reacting flows, Computational Thermal Sciences: An International Journal 1 (2) (2009) 1–24.

[26] S. Silvestri, A. Patel, D. Roekaerts, R. Pecnik, Turbulence radiation interaction in channel flow with various optical depths, Journal of Fluid Mechanics 834 (2018) 359–384.

[27] D. Edwards, Molecular gas band radiation, in: Advances in heat transfer, Vol. 12, Elsevier, 1976, pp. 115–193.

[28] Y. Zhang, R. Vicquelin, O. Gicquel, J. Taine, Physical study of radiation effects on the boundary layer structure in a turbulent channel flow, International Journal of Heat and Mass Transfer 61 (2013) 654–666.

[29] R. Vicquelin, Y. Zhang, O. Gicquel, J. Taine, Effects of radiation in turbulent channel flow: analysis of coupled direct numerical simulations, Journal of Fluid Mechanics 753 (2014) 360–401.

[30] S. Silvestri, D. Roekaerts, R. Pecnik, Assessing turbulence-radiation interactions in turbulent flows of non-gray media, Journal of Quantitative Spectroscopy and Radiative Transfer 233 (2019) 134–148.

[31] R. M. Goody, Y. L. Yung, Atmospheric radiation: theoretical basis, Oxford university press, 1995.

[32] J. Taine, A. Soufiani, Gas ir radiative properties: from spectroscopic data to approximate models, Advances in heat transfer 33 (1999) 295–414.

[33] J. Armengol, R. Vicquelin, A. Coussement, R. Santos, O. Gicquel, Scaling of heated plane jets with moderate radiative heat transfer in coupled DNS, International Journal of Heat and Mass Transfer 139 (2019) 456–474.

[34] A. A. Townsend, The structure of turbulent shear flow, Cambridge university press, 1980.

[35] S. Stanley, S. Sarkar, J. Mellado, A study of the flow-field evolution and mixing in a planar turbulent jet using direct numerical simulation, Journal of Fluid Mechanics 450 (2002) 377–407.

[36] M. Klein, A. Sadiki, J. Janicka, Investigation of the influence of the reynolds number on a plane jet using direct numerical simulation, International Journal of Heat and Fluid Flow 24 (6) (2003) 785–794.

[37] G. Lemieux, P. Oosthuizen, Experimental study of the behavior of plane turbulent jets at low reynolds numbers, AIAA journal 23 (12) (1985) 1845–1846.

[38] E. Lemmon, M. McLinden, D. Friend, Thermophysical properties of fluid systems, NIST chemistry webbook, NIST standard reference database 69.

[39] D. V. Gaitonde, M. R. Visbal, Further development of a navier stokes solution procedure based on higher-order formulas, Technical Paper 99-0557, AIAA Press.

[40] Y. Wang, A. Trouvé, Artificial acoustic stiffness reduction in fully compressible, direct numerical simulation of combustion, Combustion Theory and Modelling 8 (3) (2004) 633–660.

[41] A. Coussement, O. Gicquel, J. Caudal, B. Fiorina, G. Degrez, Three-dimensional boundary conditions for numerical simulations of reactive compressible flows with complex thermochemistry, Journal of computational physics 231 (17) (2012) 5571–5611.

[42] T. Passot, A. Pouquet, Numerical simulation of compressible homogeneous flows in the turbulent regime, Journal of Fluid Mechanics 181 (1987) 441–466.

[43] L. Palluotto, N. Dumont, P. Rodrigues, O. Gicquel, R. Vicquelin, Assessment of randomized quasi-monte carlo method efficiency in radiative heat transfer simulations, Journal of Quantitative Spectroscopy and Radiative Transfer 236 (2019) 106570.

[44] L. Tessé, F. Dupoirieux, B. Zamuner, J. Taine, Radiative transfer in real gases using reciprocal and forward monte carlo methods and a correlated-k approach, International Journal of Heat and Mass Transfer 45 (13) (2002) 2797–2814.

[45] L. Christiane, Monte Carlo and Quasi-Monte Carlo Sampling, Springer, 2008.

[46] S. Joe, F. Y. Kuo, Constructing sobol sequences with better two-dimensional projections, SIAM Journal on Scientific Computing 30 (5) (2008) 2635–2654.

[47] P. Rivière, A. Soufiani, Updated band model parameters for h2o, co2, ch4 and co radiation at high temperature, International Journal of Heat and Mass Transfer 55 (13-14) (2012) 3349–3358.

[48] A. Soufiani, J. Taine, High temperature gas radiative property parameters of statistical narrow-band model for H2O, CO2 and CO, and correlated-k model for H2O and CO2, International journal of heat and mass transfer 40 (4) (1997) 987–991.

[49] L. S. Rothman, I. E. Gordon, R. J. Barber, H. Dothe, R. R. Gamache, A. Goldman, V. I. Perevalov, S. A. Tashkun, J. Tennyson, HITEMP, the high-temperature molecular spectroscopic database, Journal of Quantitative Spectroscopy and Radiative Transfer 111 (15) (2010) 2139–2150.

[50] J. C. Del Alamo, J. Jiménez, Spectra of the very large anisotropic scales in turbulent channels, Physics of Fluids 15 (6) (2003) L41–L44.

[51] J. C. Del Alamo, J. Jiménez, P. Zandonade, R. D. Moser, Scaling of the energy spectra of turbulent channels, Journal of Fluid Mechanics 500 (2004) 135–144.

[52] S. Mazumder, M. F. Modest, Turbulence-radiation interactions in nonreactive flow of combustion gases, Transactions-American Society of Mechanical Engineers Journal of Heat Transfer 121 (1999) 726–728.

[53] G. Fraga, F. Centeno, A. Petry, F. França, Evaluation and optimization-based modification of a model for the mean radiative emission in a turbulent non-reactive flow, International Journal of Heat and Mass Transfer 114 (2017) 664–674.